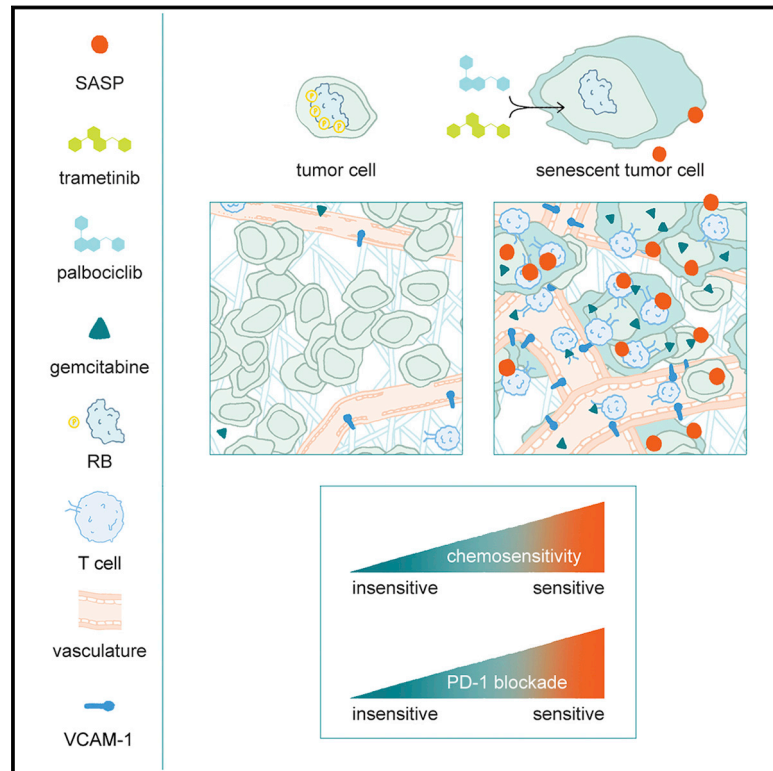# Cell

Senescence-Induced Vascular Remodeling Creates Therapeutic Vulnerabilities in Pancreas Cancer

Graphical Abstract

Authors

Marcus Ruscetti, John P. Morris IV, Riccardo Mezzadra, ..., Ben Z. Stanger, Charles J. Sherr, Scott W. Lowe

Correspondence

lowes@mskcc.org

In Brief

In mouse models of KRAS mutant pancreatic ductal adenocarcinoma, tumor cell senescence following MEK and CDK4/6 inhibition promotes vascular remodeling through induction of a pro-angiogenic senescence-associated secretory phenotype, leading to enhanced drug delivery and T cell infiltration that sensitizes these tumors to chemotherapy and immune checkpoint blockade.

Highlights

- Therapy-induced senescence in PDAC triggers SASP-dependent vascular remodeling

- SASP-mediated vascularization facilitates chemotherapy uptake and efficacy

- SASP-mediated endothelial activation drives T cell infiltration into PDAC lesions

- Senescence-inducing treatment potentiates PD-1 blockade in PDAC models

CellPress

Senescence-Induced Vascular Remodeling Creates Therapeutic Vulnerabilities in Pancreas Cancer

Marcus Ruscetti,[1,10] John P. Morris IV,[1,10] Riccardo Mezzadra,[1,10] James Russell,[2] Josef Leibold,[1] Paul B. Romesser,[3] Janelle Simon,[1] Amanda Kulick,[4] Yu-jui Ho,[1] Myles Fennell,[1] Jinyang Li,[5] Robert J. Norgard,[5] John E. Wilkinson,[6] Direna Alonso-Curbelo,[1] Ramya Sridharan,[4,7] Daniel A. Heller,[4,7] Elisa de Stanchina,[4] Ben Z. Stanger,[5] Charles J. Sherr,[8] and Scott W. Lowe[1,9,11,*]

[1]Department of Cancer Biology and Genetics, Memorial Sloan Kettering Cancer Center, New York, NY 10065, USA
[2]Department of Medical Physics, Memorial Sloan Kettering Cancer Center, New York, NY 10065, USA
[3]Department of Radiation Oncology, Memorial Sloan Kettering Cancer Center, New York, NY 10065, USA
[4]Department of Molecular Pharmacology, Memorial Sloan Kettering Cancer Center, New York, NY 10065, USA
[5]Perelman School of Medicine, University of Pennsylvania, Philadelphia, PA 19104, USA
[6]Department of Pathology, University of Michigan School of Medicine, Ann Arbor, MI 48109, USA
[7]Weill Cornell Medical College, Cornell University, New York, NY 10065, USA
[8]Department of Tumor Cell Biology, St. Jude Children's Research Hospital, Memphis, TN 38105, USA
[9]Howard Hughes Medical Institute, Chevy Chase, MD 20815, USA
[10]These authors contributed equally
[11]Lead Contact
*Correspondence: lowes@mskcc.org
https://doi.org/10.1016/j.cell.2020.03.008

SUMMARY

KRAS mutant pancreatic ductal adenocarcinoma (PDAC) is characterized by a desmoplastic response that promotes hypovascularity, immunosuppression, and resistance to chemo- and immunotherapies. We show that a combination of MEK and CDK4/6 inhibitors that target KRAS-directed oncogenic signaling can suppress PDAC proliferation through induction of retinoblastoma (RB) protein-mediated senescence. In preclinical mouse models of PDAC, this senescence-inducing therapy produces a senescence-associated secretory phenotype (SASP) that includes pro-angiogenic factors that promote tumor vascularization, which in turn enhances drug delivery and efficacy of cytotoxic gemcitabine chemotherapy. In addition, SASP-mediated endothelial cell activation stimulates the accumulation of CD8+ T cells into otherwise immunologically "cold" tumors, sensitizing tumors to PD-1 checkpoint blockade. Therefore, in PDAC models, therapy-induced senescence can establish emergent susceptibilities to otherwise ineffective chemo- and immunotherapies through SASP-dependent effects on the tumor vasculature and immune system.

INTRODUCTION

Pancreatic ductal adenocarcinoma (PDAC) conveys a dismal prognosis (Siegel et al., 2019) and is refractory to chemo- and immunotherapies, including immune checkpoint blockade that has revolutionized the treatment landscape of other tumors (Ribas and Wolchok, 2018; Royal et al., 2010). This treatment-re-fractory behavior likely results from the unique characteristics of PDAC, which arises through perturbations in a combination of undruggable cancer drivers, including mutations in the KRAS oncogene and disruption of the TP53, SMAD4, and CDKN2A tumor suppressors (Morris et al., 2010). Furthermore, the disease evolves within a heterogeneous tumor microenvironment (TME) characterized by a fibro-inflammatory stroma that contributes to disease progression (Ligorio et al., 2019; Öhlund et al., 2017), limits drug accessibility (Olive et al., 2009; Provenzano et al., 2012), and enforces an immune suppressive niche that suppresses anti-tumor immunity (Kraman et al., 2010). Indeed, several strategies have targeted aspects of the PDAC TME to improve drug uptake (Chauhan et al., 2013; Olive et al., 2009; Provenzano et al., 2012) and sensitivity to immunotherapies (Feig et al., 2013; Jiang et al., 2016).

KRAS mutations occur in over 90% of human PDAC, and mouse models implicate oncogenic KRAS in initiating and maintaining tumorigenesis as well as the stromal changes that accompany disease progression (Collins et al., 2012a, 2012b; Kapoor et al., 2014). While pharmacological efforts to directly target KRAS or its downstream effectors have proven largely ineffective to date, combinatorial strategies for inhibiting RAS pathway components and interfering with compensatory or negative feedback signaling have shown promise in preclinical studies (Manchado et al., 2016; Okumura and Jänne, 2014; Sun et al., 2014). Recently, we demonstrated that one of these targeted therapy combinations—the MEK inhibitor trametinib and CDK4/6 inhibitor palbociclib—could lead to durable cell-cycle exit of KRAS mutant lung and pancreas cancer cells through induction of retinoblastoma (RB) protein-mediated cellular senescence (Ruscetti et al., 2018).

Cellular senescence is a physiological stress-response that results in the proliferative arrest and immune-mediated clearance of damaged and pre-malignant cells, seemingly as a part of a wound healing process that facilitates tissue regeneration after injury (Demaria et al., 2014; Kang et al., 2011; Krizhanovsky

et al., 2008; Mosteiro et al., 2016). Senescence can be triggered by oncogenic signaling, including by mutant KRAS in pre-malignant lesions such as pancreatic intraepithelial neoplasias (PanINs) (Caldwell et al., 2012), thus serving as a natural barrier to malignancy. The CDKN2A/RB and p53 tumor suppressor programs collaborate to regulate this process, and their disruption can disable senescence and facilitate cancer initiation and progression, including in PDAC (Bardeesy et al., 2006; Carrière et al., 2011; Morton et al., 2010; Serrano et al., 1997).

Two key molecular modules involved in senescence are an RB-dependent program that produces a repressive chromatin state to transcriptionally silence many pro-proliferative genes (Chicas et al., 2010; Narita et al., 2003), and a nuclear factor κB (NF-κB)-regulated gene activation program that induces expression of secreted factors that can influence the microenvironment (Chien et al., 2011; Lesina et al., 2016; Tasdemir et al., 2016). This latter component is often referred to as the senescence-associated secretory phenotype (SASP) and is characterized by the secretion of chemokines, cytokines, matrix metalloproteinases (MMPs), and other paracrine signaling factors (Coppé et al., 2008; Kuilman and Peeper, 2009). Given the pleiotropic nature of many of these secreted factors, the consequences of SASP are context-dependent, and can influence multiple cell types within the tumor milieu (Coppé et al., 2010; Faget et al., 2019). Hence, while SASP factors can be pro- or anti-tumorigenic, their production by pre-malignant cells can stimulate immune surveillance, leading to the clearance of senescent cells and contributing to tumor suppression (Kang et al., 2011; Tasdemir et al., 2016).

Although cancer cells evade senescence early during the course of tumor evolution, restoration of this program in advanced cancers can have profound anti-tumor effects. Indeed, genetic restoration of p53 in a RAS-driven liver carcinoma model induces senescence to promote tumor clearance by triggering innate immune surveillance (Xue et al., 2007). Pharmacological strategies that induce tumor cell senescence can also facilitate anti-tumor immunity and tumor regressions despite the absence of cytotoxicity to cancer cells themselves. For example, in a KRAS mutant lung cancer model, the induction of senescence by trametinib and palbociclib treatment triggered SASP-dependent and natural killer (NK) cell-mediated tumor regressions, even in tumors lacking p53 (Ruscetti et al., 2018). Intrigued by the ability of these RAS pathway-targeted therapies to produce therapeutically relevant effects on the surrounding TME, we set out to explore how senescence induction could remodel the hypovascular and immune suppressive PDAC TME and alter the treatment landscape of this disease.

RESULTS

Trametinib and Palbociclib Treatment Triggers Vascular Remodeling in PDAC
Combined trametinib and palbociclib (T/P) treatment, but neither agent alone, potently induces senescence and SASP in human PDAC lines (Ruscetti et al., 2018). To determine if therapy-induced senescence can alter the PDAC TME, we evaluated the response to T/P treatment in two mouse models of PDAC that recapitulate the histopathology and stromal responses observed clinically: the *Pdx1-Cre;LSL-KRAS^{G12D};Trp53^{fl/wt}* (*KPC^{flox}*) genetically engi-

neered mouse model (GEMM), where tumors form autochthonously in the pancreas (Herreros-Villanueva et al., 2012); and orthotopic transplantation of PDAC organoids derived from tumors arising in *Pdx1-Cre; LSL-KRAS^{G12D};Trp53^{R172H/wt}* (*KPC^{mut}*) mice into the pancreata of syngeneic C57BL/6 recipients (Boj et al., 2015; Hingorani et al., 2003).

Two-week treatment with T/P (but neither agent alone) led to decreased proliferation, inhibition of ERK and RB phosphorylation, and induction of senescence-associated β-galactosidase (SA-β-gal) activity in the absence of apoptosis in both *KPC^{flox}* GEMM and *KPC^{mut}* organoid transplant models (Figures 1A, S1A, and S1B). This response was associated with a modest increase in the survival of PDAC-bearing animals (Figures S1C and S1D). In contrast to KRAS-driven lung cancer models (Ruscetti et al., 2018), however, T/P treatment did not increase NK cell numbers, activation, or cytotoxicity, and failed to elicit tumor regressions (Figures S1B and S1E–S1H). Therefore, while T/P treatment triggers senescence in PDAC, this does not engage NK cell surveillance or produce robust tumor regressions.

Close inspection of T/P-treated tumor sections showed an accumulation of blood vessels adjacent to tumor cells (Figure 1B), suggesting that T/P therapy may affect the TME in other ways. Combinatorial treatment led to an increase in CD31+ blood vessel density and closer proximity of vessels and tumor cells in both organoid transplant and GEMM models (Figures 1B, 1C, S1I, and S1J). By contrast, no change in the number of lymphatic vessels was observed (Figure S1L). Although many blood vessels in vehicle-treated PDAC tumors appeared collapsed, most in T/P-treated tumors harbored open and readily discernible lumens (Figures 1B, 1D, S1I, and S1K). T/P treatment also reduced the stromal content of hyaluronic acid (HA), an effect linked to increased vessel opening in PDAC (Provenzano et al., 2012), without affecting collagen deposition or accumulation of α-smooth muscle actin (αSMA)-positive myofibroblasts (Figures 1B, S1M, and S1N). Whereas the improved vascularization achieved through inhibition of signaling pathways involved in maintaining the desmoplastic stroma is associated with increased metastasis (Lee et al., 2014; Rhim et al., 2014), PDAC-bearing mice treated with T/P showed fewer metastases compared to controls (Figures S1O and S1P). Hence, T/P treatment induces vascular remodeling without metastatic adaptation.

Compared to controls, the blood vessels present in T/P-treated tumors were associated with higher levels of αSMA and the pericyte marker PDGFRβ, characteristics of a mature vasculature (Figures 1E, 1F, and S1Q). Vascular endothelial cells also displayed upregulation of immunomodulatory cell surface molecules such as P-selectin, VCAM-1, and ICAM-1 (a phenomenon hereafter referred to as endothelial cell activation) that are expressed on permeable blood vessels that accompany tissue inflammation (Figures 1G, 1H, S1R, and S1S) (Hunt and Jurd, 1998; Lorenzon et al., 1998). Therefore, T/P treatment, perhaps by promoting senescence, leads to multiple vascular remodeling phenotypes in PDAC models.

SASP Factors Contribute to Vascular Remodeling in PDAC
In addition to immunomodulatory factors, senescent cells secrete SASP factors that can alter endothelial cell proliferation
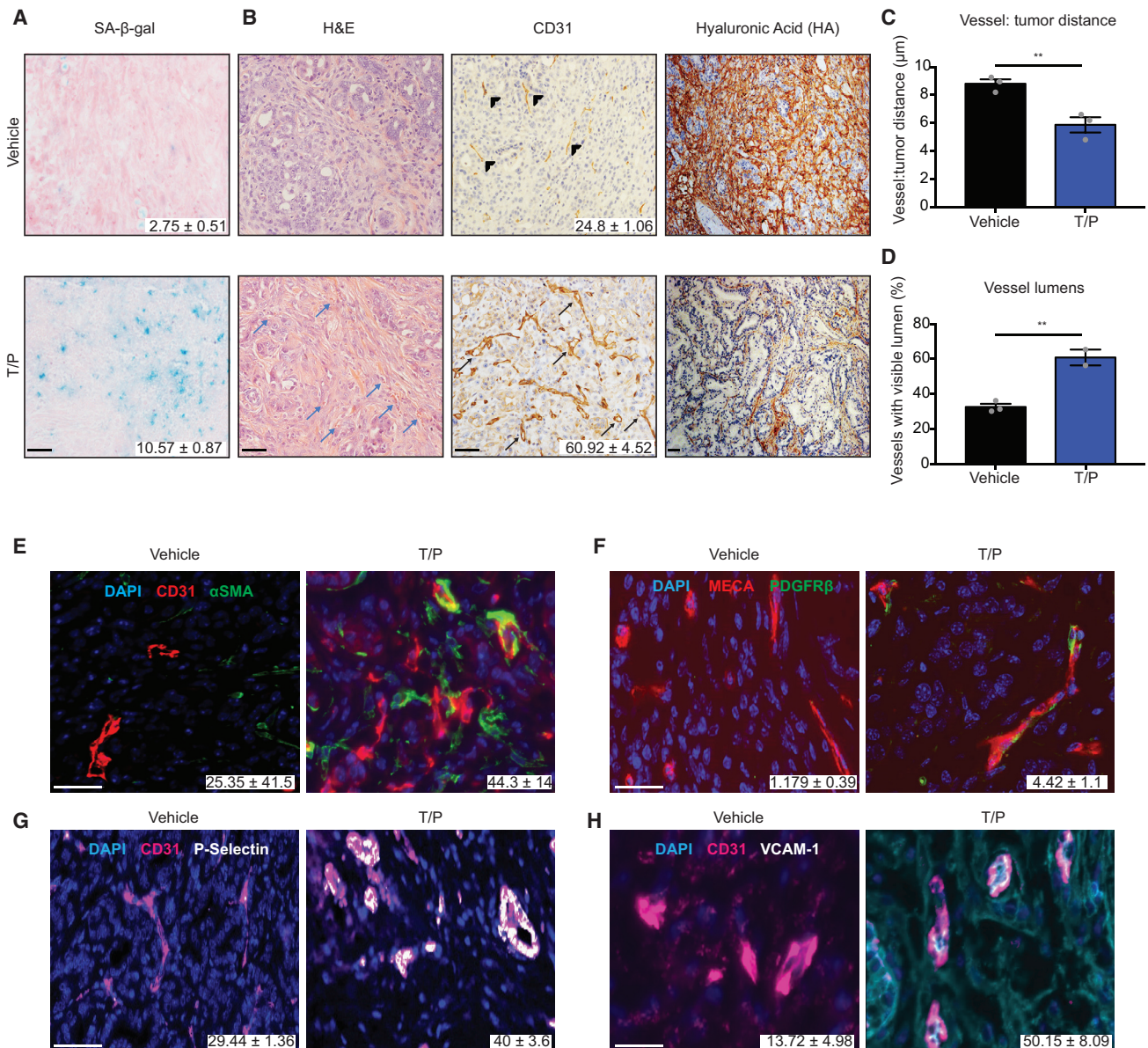
Figure 1. Trametinib and Palbociclib Treatment Triggers Vascular Remodeling in PDAC

(A and B) H&E and immunohistochemical (IHC) staining of *KPC^flox* GEMM tumors treated with vehicle or trametinib (1 mg/kg) and palbociclib (100 mg/kg) for 2 weeks. Quantification of SA-β-gal positive area (A) and blood vessels per field (B) are shown (n = 2–3; p < 0.02). Blue arrow, blood vessel; arrowhead, collapsed vessel; black arrow, visible lumen.

(C) Analysis of distance between vessels and tumor cells in (B) (n = 3).

(D) Quantification of vessels with visible lumens in (B) (n = 3).

(E–H) Immunofluorescence (IF) staining and quantification of αSMA (E), PDGFRβ (F), P-selectin (G), and VCAM-1 (H) colocalization with blood vessels in *KPC^flox* GEMM tumors treated as in (A) (n = 2–3; p = 0.021, 0.044, 0.111, and 0.062, respectively).

Error bars, mean ± SEM. **p < 0.01. Scale bars, 50 μm.

See also Figure S1.

and behavior (Ancrile et al., 2007; Coppé et al., 2006; Mikuła-Pietrasik et al., 2016; Oubaha et al., 2016). Indeed, murine and human PDAC lines treated with T/P displayed increased secretion of pro-angiogenic factors (VEGF, PDGFA/B, FGF2) and MMPs (MMP2/3/7/9/10) compared to cells treated with single agents (Figures 2A and S2A). Increased expression of these

SASP factors was also detected in tumor cells sorted from T/P-treated tumors derived from orthotopic transplant of *KPC^mut* cell lines engineered to express luciferase and GFP, and conditioned media from *KPC^mut* cells pretreated with T/P was able to support the proliferation of endothelial cells in culture (Figures 2B, S2B, and S2C). Similarly, when endothelial cells were grown
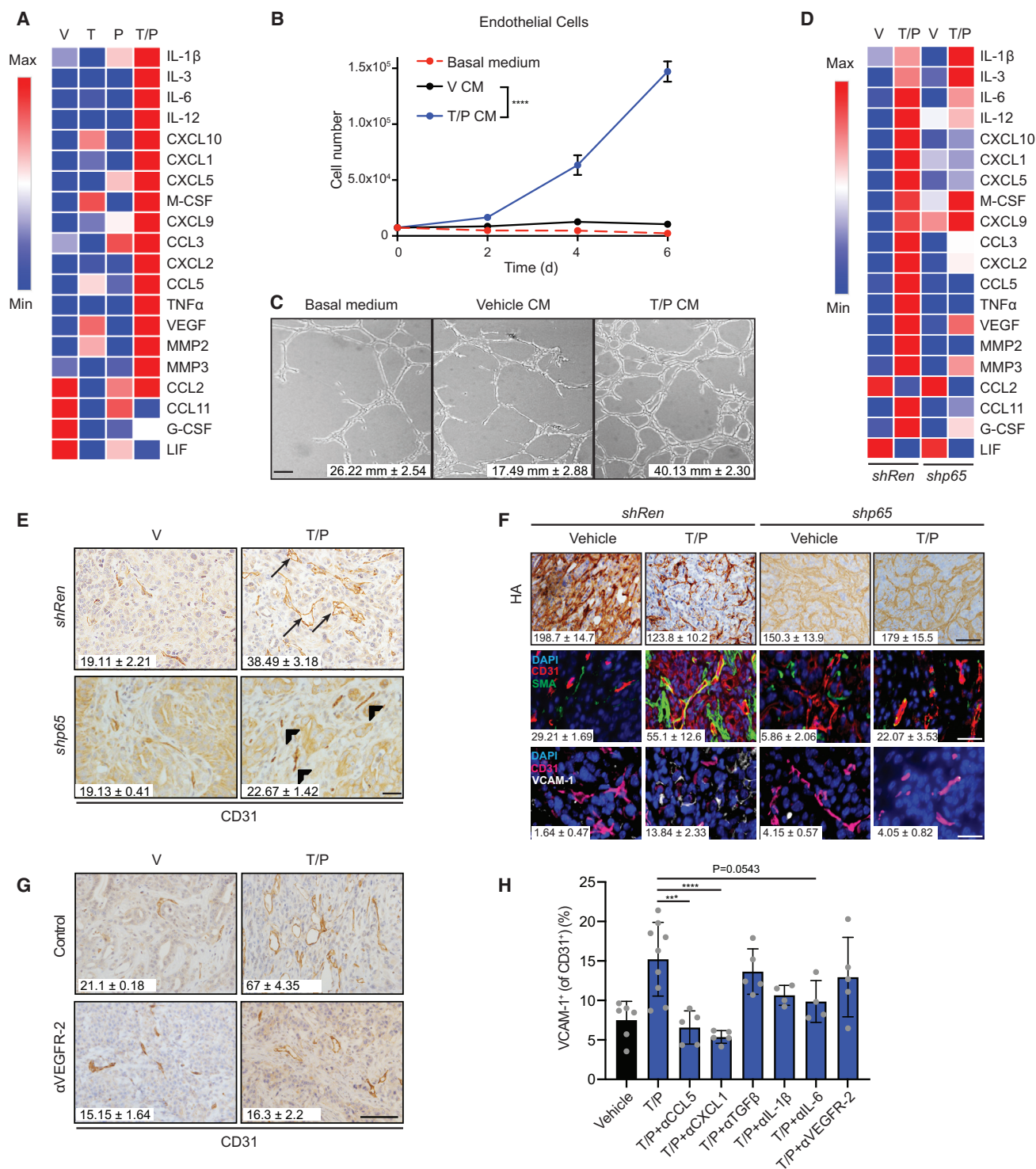
Figure 2. SASP Factors Contribute to Vascular Remodeling in PDAC

(A) Heatmap of cytokine array results from *KPC^{mut}* cells following 8-day treatment with trametinib (25 nM) and/or palbociclib (500 nM). Data presented as mean of three biological replicates.

(B) Cell growth analysis of 3B11 cells cultured in serum-free (basal) or conditioned media (CM) from *KPC^{mut}* cells treated as in (A) (n = 3).

(C) Endothelial tube formation analysis of 3B11 cells cultured in CM from (B). Quantification of total tube length is shown (n = 2; V versus T/P, p = 0.01).

(D) Heatmap of cytokine array results from *KPC^{mut}* cells harboring control *Renilla* (*Ren*) or *p65* shRNAs and treated as in (A). Data presented as mean of three biological replicates.

(legend continued on next page)

on a 3D basement membrane, conditioned media from T/P-treated KPC^{mut} cells promoted the formation of tube-like structures that were reminiscent of vascular networks *in vivo* (Figure 2C).

Other stromal subtypes in the PDAC TME, most prominently fibroblasts and macrophages, can also secrete factors that promote angiogenesis. However, T/P treatment did not stimulate the secretion of angiogenic factors from pancreatic fibroblasts, and conditioned media from T/P-treated senescent PDAC cells did not affect fibroblast or macrophage proliferation (Figures S2D–S2F). While there was an increase in the number of PDAC-associated F4/80$^+$ macrophages and their expression of MHC-II and CD86 following T/P treatment, we only observed minor changes in expression of VEGF or other macrophage polarization markers (Figures S2G–S2I). Furthermore, the vascular remodeling that accompanied senescence induction was not dependent on immune cells, as T/P treatment of tumors derived from KPC^{mut} organoids injected orthotopically into C567BL/6 or immunodeficient NOD-*scid* IL2Rγ^{null} (NSG) mice led to similar increases in vascular density, open vessel lumens, and endothelial activation (Figures S2J–S2L). Therefore, senescent tumor cells are likely the primary source of angiogenic SASP factors following T/P treatment.

To directly test whether the SASP contributes to vascular remodeling *in vivo*, KPC^{mut} organoids were transduced with short hairpin RNAs (shRNAs) targeting the p65 subunit of NF-κB, a transcription factor required for SASP induction but dispensable for senescence-mediated growth arrest (Chien et al., 2011; Ruscetti et al., 2018). As predicted, suppression of NF-κB in PDAC cells treated with T/P reduced the secretion of both immune modulatory and pro-angiogenic SASP factors (Figure 2D). KPC^{mut} organoids expressing the *p65* or control (*Ren*) shRNA were then transplanted orthotopically into C57BL/6 mice to assess the impact of SASP suppression on vascular remodeling. While potent NF-κB inhibition can block proliferation of KRAS mutant tumors in some contexts (Lesina et al., 2016; Meylan et al., 2009), partial NF-κB suppression using p65-targeting shRNAs did not affect tumor growth or senescence-associated cell-cycle arrest of KPC^{mut} organoid-derived tumors following T/P treatment (Figures S3A–S3C). Instead, p65 suppression blocked the increase in vascular density, maturation, perfusion, and immunomodulatory activation, as well as the decrease in HA levels that accompanies T/P treatment in tumors harboring *Ren* shRNAs (Figures 2E, 2F, and S3D–S3H).

VEGF was one SASP factor that contributed to vascular remodeling. Treatment of human and murine PDAC cells produced an NF-κB-dependent increase in VEGF secretion (Figures 2A,

2D, and S2A). Moreover, suppression of VEGFR-2, the cognate receptor for VEGF, using high doses of the VEGFR-2 blocking antibody DC101 effectively inhibited neo-vascularization following T/P treatment (Figure 2G). By contrast, VEGFR-2 blockade did not inhibit the upregulation of endothelial activation markers P-selectin and VCAM-1 following T/P treatment, which instead were suppressed using antagonizing antibodies against other inflammatory SASP factors, including CCL5, CXCL1, and interleukin (IL)-6 (Figures 2H and S3I). Thus, different SASP factors collaborate to produce vascular remodeling and endothelial cell activation after T/P treatment.

Senescence-Inducing Therapies Sensitize PDAC to Cytotoxic Chemotherapy

The hypovascularity and vascular compression associated with PDAC contributes to its chemo-refractory nature by impeding drug delivery to the tumor (Olive et al., 2009; Provenzano et al., 2012). To determine if SASP-mediated vascular remodeling enhances tumor perfusion and permeability of soluble factors, including standard-of-care gemcitabine chemotherapy, tumor-bearing KPC^{mut} organoid transplant or KPC^{flox} GEMM mice were pretreated with vehicle or T/P for 2 weeks, and then injected with (1) lectin, (2) a high molecular weight dextran, and/or (3) a ^{14}C-labeled gemcitabine radiotracer. Consistent with the increase in vessel size and maturation, vessels in T/P pretreated tumors had increased lectin perfusion (Figure 3A). T/P pretreated tumors also had significantly more dextran accumulation as compared to controls, indicative of enhanced vessel permeability (Figures 3A and S4B). These dual effects of T/P treatment on vascular permeability and perfusion resulted in no change in hypoxia in the PDAC TME as assessed by pimonidazole staining (Figure S4A).

T/P pretreatment also increased gemcitabine penetration into the tumor, particularly in focal regions containing high densities of SA-β-gal$^+$ senescent cells and blood vessels (Figures 3A, 3B, and S4B). By contrast, such effects were not observed in the normal pancreas or other organs of the same tumor-bearing mice (Figure S4C). The increase in drug uptake and dextran accumulation in tumors following T/P treatment was suppressed upon tumor-specific *p65* knockdown or DC101 treatment, indicating these processes were dependent on SASP induction and signaling through the SASP factor VEGF (Figures 3B and S4D).

To assess whether the addition of gemcitabine to the T/P combination (T/P/G) produced better treatment outcomes than either regimen alone, cohorts of tumor-bearing KPC^{mut} organoid transplant or KPC^{flox} GEMM mice were monitored for tumor response and for overall survival following treatment with gemcitabine,

(E) IHC staining and quantification of blood vessels per field in KPC^{mut} organoid transplant tumors harboring *Ren* or *p65* shRNAs and treated for 2 weeks with vehicle or trametinib (1 mg/kg) and palbociclib (100 mg/kg) (n = 3; *Ren* T/P versus *p65* T/P, p = 0.003). Arrowhead, collapsed vessel; arrow, visible lumen.
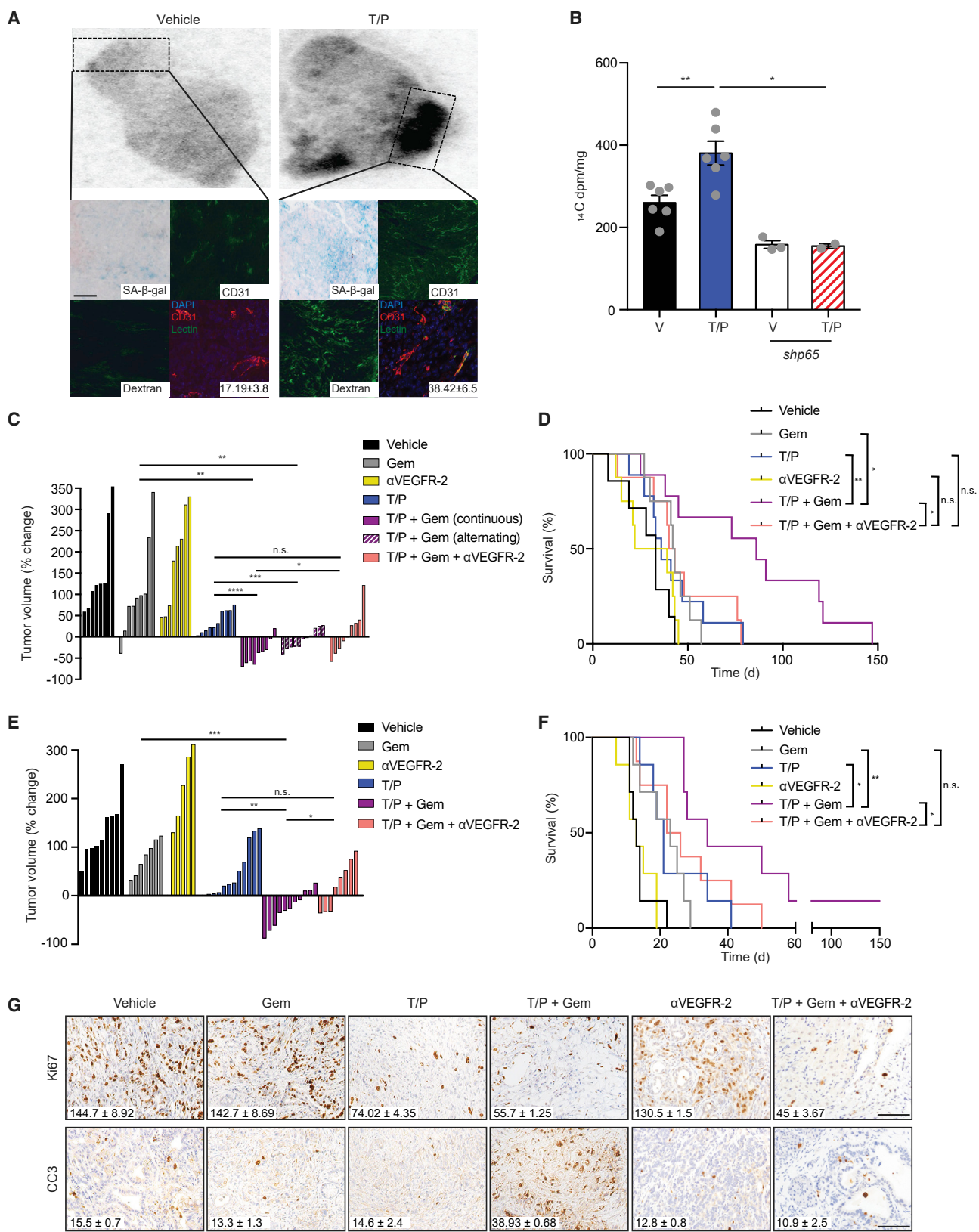
(F) IHC and IF staining of tumor samples in (E). Quantification of HA staining and αSMA and VCAM-1 colocalization with blood vessels are shown (n = 2–3; *Ren* V versus *Ren* T/P, p ≤ 0.05; *Ren* T/P versus *p65* T/P, p ≤ 0.05).

(G) IHC staining and quantification of blood vessels per field in KPC^{mut} organoid transplant tumors treated for 2 weeks with vehicle, trametinib (1 mg/kg), palbociclib (100 mg/kg), and/or a VEGFR-2 blocking antibody (DC101; 800 μg) (n = 3; T/P versus T/P+DC101, p = 0.003).

(H) Flow cytometry analysis of VCAM-1 expression on endothelial cells in KPC^{mut} cell transplant tumors treated with vehicle, trametinib (1 mg/kg), palbociclib (100 mg/kg), and/or monoclonal antibodies (mAbs) targeting CCL5 (MAB478; 50 μg), CXCL1 (MAB453; 25 μg), TGF-β (1D11; 300 μg), IL-1β (B122; 200 μg), IL-6 (MP5-20F3; 200 μg), or VEGFR-2 (DC101; 800 μg) for 2 weeks (n ≥ 4).

Two-way ANOVA (B). One-way ANOVA (F and H). Error bars, mean ± SEM. ****p < 0.001, ***p < 0.01, Scale bars, 50 μm.

See also Figures S2 and S3.

A Vehicle | T/P

SA-β-gal | CD31

DAPI CD31 Lectin

Dextran | 17.19±3.8

SA-β-gal | CD31

DAPI CD31 Lectin

Dextran | 38.42±6.5

B

C

- Vehicle
- Gem
- αVEGFR-2
- T/P
- T/P + Gem (continuous)
- T/P + Gem (alternating)
- T/P + Gem + αVEGFR-2

D

- Vehicle
- Gem
- T/P
- αVEGFR-2
- T/P + Gem
- T/P + Gem + αVEGFR-2

E

- Vehicle
- Gem
- αVEGFR-2
- T/P
- T/P + Gem
- T/P + Gem + αVEGFR-2

F

- Vehicle
- Gem
- T/P
- αVEGFR-2
- T/P + Gem
- T/P + Gem + αVEGFR-2

G Vehicle | Gem | T/P | T/P + Gem | αVEGFR-2 | T/P + Gem + αVEGFR-2

Ki67
144.7 ± 8.92 | 142.7 ± 8.69 | 74.02 ± 4.35 | 55.7 ± 1.25 | 130.5 ± 1.5 | 45 ± 3.67

CC3
15.5 ± 0.7 | 13.3 ± 1.3 | 14.6 ± 2.4 | 38.93 ± 0.68 | 12.8 ± 0.8 | 10.9 ± 2.5

(legend on next page)

T/P, or both. To examine the contribution of the remodeled vasculature to drug activity, some mice were also treated with DC101 to prevent SASP-mediated neo-vascularization. As is often observed clinically (Carmichael et al., 1996), gemcitabine alone had modest effects on tumor growth and limited survival impact in our murine PDAC models (Figures 3C–3F). T/P treatment modestly delayed tumor growth and produced a marginal survival advantage, but the T/P/G regimen produced potent tumor regressions and significantly enhanced survival, effects that were largely ablated by DC101 (Figures 3C–3F). Similar efficacy was observed when PDAC-bearing mice were treated using an alternating weekly schedule of T/P and gemcitabine (Figures 3C). These results further support a role for T/P pretreatment in priming gemcitabine efficacy through its vascular remodeling effects, as has been observed in other settings (Olive et al., 2009; Provenzano et al., 2012).

Histological analyses of tumors revealed that T/P or gemcitabine treatment alone was not cytotoxic, but the T/P/G regimen produced considerable tumor cell apoptosis that could be blocked by DC101 (Figures 3G, S4E, and S4F). We suspect that this increase in tumor cell apoptosis results from a culling of cycling tumor cells that fail to senesce, as analysis of the residual tumor mass following short-term T/P/G treatment revealed an enrichment for non-proliferating and SA-β-gal-positive cells as compared to T/P or gemcitabine treatment alone (Figures 3G and S4E–S4G). Thus, SASP-provoked vascular remodeling can enhance PDAC responses to cytotoxic chemotherapy, at least in part, by facilitating drug uptake.

We also examined the treatment responses of two patient-derived xenograft (PDX) models propagated through subcutaneous transplantation of PDAC tissue into immunodeficient mice. While many subcutaneous xenograft models lack the dense stroma and hypovascularity found in autochthonous PDACs (Olive et al., 2009), two models obtained from patients that had progressed under gemcitabine chemotherapy regimens retained a robust and dense stroma and thus were chosen for further analysis (Figure S4H). As was noted in the murine models, T/P treatment triggered proliferative arrest and senescence in PDX tumors, together with an increase in vascular density and lumen diameter and HA degradation in the stroma (Figures S4H–S4K). Both PDX models had only a modest response to gemcitabine alone, whereas T/P/G therapy produced an increase in apoptosis associated with sustained tumor growth

inhibition and partial tumor regressions in some mice (Figures S4L–S4N). Thus, vascular remodeling following therapy-induced senescence also sensitizes human PDAC to chemotherapy.

The SASP Promotes T Cell Infiltration via Endothelial Activation

Besides its dysfunctional vasculature, human and mouse PDAC displays an abundance of immune suppressive myeloid and regulatory T cells (T_{regs}) together with a scarcity of cytotoxic lymphocytes (Blando et al., 2019; Clark et al., 2007; Vonderheide and Bayne, 2013). As such, these tumors are considered immunologically "cold." Hypovascularity and lack of an activated endothelium can also impair lymphocyte homing to normal and malignant tissues (Huang et al., 2018; Muller, 2009; Wu et al., 1992). We therefore used a combination of genetic and pharmacological approaches to assess the consequences of perturbing SASP, neo-vascularization, or endothelial cell activation on immune cell infiltrates following T/P therapy.

Consistent with the above results (see Figures S1E and S1F), drug treatment did not increase NK cell numbers or activity in any of the three murine PDAC models tested, and antibody-mediated NK cell depletion did not affect the survival of T/P-treated mice harboring orthotopically transplanted KPC^{mut} cell-derived tumors (Figures S5A and S5B). Instead, we noted a substantial increase in the influx of T cells, and in particular, CD8$^+$ T cells, into the tumor mass of transplanted and autochthonous PDAC following 2-week T/P treatment (Figures 4A, 4B, and S5C). Immunophenotyping confirmed that this increase was mainly due to CD8$^+$ T cell accumulation that occurred in the absence of changes in Ly6G$^+$ neutrophil, Gr-1^{hi}CD11b$^+$ myeloid-derived suppressor cell (MDSC), FOXP3$^+$ T_{reg}, or FAP$^+$ fibroblast populations that have been associated with CD8$^+$ T cell suppression in PDAC (Figures 4C, 4D, and S5D–S5F) (Clark et al., 2007; Feig et al., 2013; Jiang et al., 2016; Steele et al., 2016). This T/P treatment-induced increase in CD8$^+$ T cells required SASP-mediated vascular remodeling, as the effect was largely abolished in tumors harboring a *p65* shRNA or treated with DC101 (Figures 4E–4H).

To assess whether endothelial cell activation contributes to CD8$^+$ T cell accumulation that accompanies senescence in T/P-treated PDAC, we used neutralizing antibodies against the P-selectin ligand PSGL-1, VCAM-1, and ICAM-1, and evaluated the PDAC immune landscape. Blockade of VCAM-1, but not

---

Figure 3. Senescence-Inducing Therapies Sensitize PDAC to Cytotoxic Chemotherapy

(A) KPC^{mut} organoid transplant mice were pretreated with vehicle or trametinib (1 mg/kg) and palbociclib (100 mg/kg) for 2 weeks and subsequently injected with ^{14}C-labeled gemcitabine (gem), dextran, and/or lectin prior to tissue harvest. Autoradiograph showing distribution of ^{14}C-gem in tumors. Below: overlay of autoradiographs with IHC/IF staining and quantification of lectin colocalization with blood vessels (n = 2–3; p = 0.054).

(B) ^{14}C-gem quantification in indicated tumors (n = 3–6).

(C) Waterfall plot of the response of KPC^{mut} organoid transplant tumors after 2 weeks treatment with vehicle, trametinib (1 mg/kg), palbociclib (100 mg/kg), gemcitabine (100 mg/kg), and/or a VEGFR-2 blocking antibody (DC101; 800 μg) either continuously or on an alternating schedule (n ≥ 8).

(D) Kaplan-Meier survival curve of KPC^{mut} organoid transplant mice treated as in (C) (n ≥ 7).

(E) Waterfall plot of the response of KPC^{flox} GEMM tumors following treatment as in (C) (n ≥ 5).

(F) Kaplan-Meier survival curve of KPC^{flox} GEMM mice treated as in (C) (n ≥ 7).

(G) IHC staining of KPC^{flox} GEMM tumors treated as in (C). Quantification of Ki67$^+$ and cleaved capase-3 (CC3$^+$) cells per field is shown (n = 3; Gem versus T/P/G and T/P/G versus T/P/G/DC101, p < 0.05).

One-way ANOVA (B, C, and E). Log-rank test (D and F). Error bars, mean ± SEM. ****p < 0.001, ***p < 0.01, **p < 0.01, *p < 0.05. n.s., not significant. Scale bars, 50 μm.

See also Figure S4.
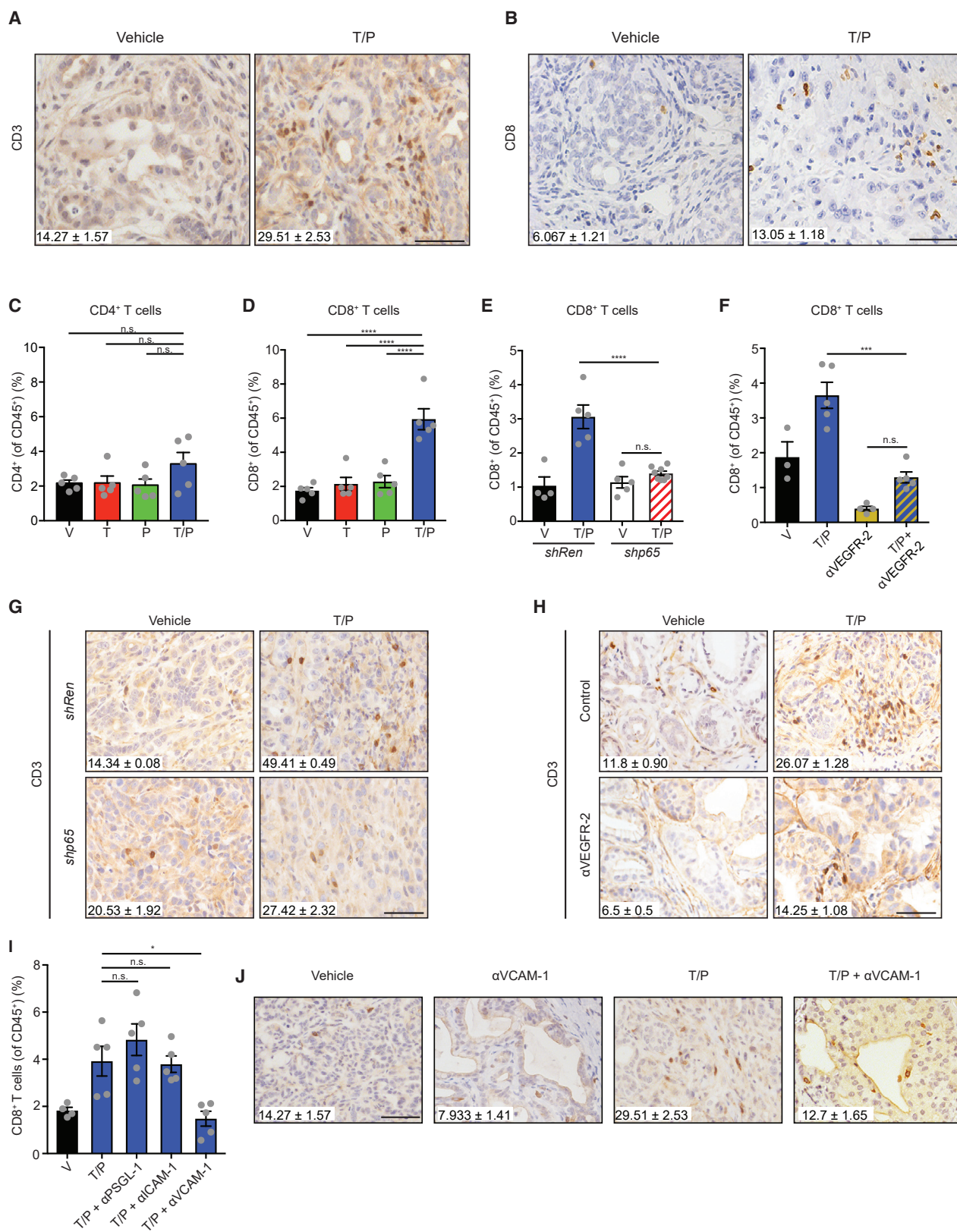
PSGL-1 or ICAM-1, significantly reduced the numbers of total and CD8+ tumor-infiltrating T cells in T/P treated-mice (Figures 4I and 4J). VCAM-1 induction on endothelial cells facilitates blood vessel adhesion and tissue extravasation of T cells expressing its ligand, VLA-4 (Lorenzon et al., 1998; Nandi et al., 2004). Accordingly, VLA-4 expression was elevated on CD8+ T cells isolated from transplanted PDAC in a SASP-dependent manner following T/P treatment (Figure S5G). Thus, SASP-induced vascular remodeling, in part through the VCAM-1/VLA-4 cell adhesion axis, enables the penetration of CD8+ T cells into the PDAC TME.

Therapy-Induced Senescence Leads to T Cell Activation and Exhaustion

PDAC-associated CD8+ T cells expressed higher levels of the activation markers CD69 and CD44 following T/P, but not single agent or vehicle treatment (Figures 5A and 5B). This effect was dependent on SASP-mediated vascular remodeling (Figures S6A–S6D), hinting that senescence induction in tumor cells may stimulate the activity of tumor-reactive T cells. Of note, both MEK and CDK4/6 inhibitors can increase antigen presentation and T cell targeting of tumor cells in other cancer models (Brea et al., 2016; Deng et al., 2018; Ebert et al., 2016; Goel et al., 2017; Schaer et al., 2018) and, accordingly, transcripts encoding components of the antigen processing/presentation machinery were elevated in human PDAC lines following T or P treatment alone (Figure S6E). Nonetheless, the T/P combination produced a much greater increase in the expression of these genes as well as surface level expression of MHC-I in orthotopic KPC^{mut} tumors (Figures 5C and S6E). This effect appeared functionally meaningful, as OT-1 T cells co-cultured with antigen matched ovalbumin (OVA)-expressing KPC^{mut} PDAC cells showed enhanced T cell activation and expression of the effector cytokines tumor necrosis factor alpha (TNF-α) and interferon (IFN)-γ after T/P-pretreatment of tumor cells in an MHC-I-dependent manner (Figures S6F and S6G).

Despite producing conditions that favor activation of cytotoxic T cell effector functions, T/P treatment did not stimulate robust anti-tumor T cell immunity in PDAC. Hence, T cells isolated from KPC^{mut} tumors following T/P treatment did not express the cytotoxicity marker CD107a, and neither CD8 nor CD4 depletion altered the modest survival advantage produced

by T/P therapy (Figures 5D and 5E). In agreement, CD8+ T cells isolated from the T/P treatment cohort displayed higher expression levels of the exhaustion markers PD-1, 2B4, CTLA-4, and LAG3 (Figure 5F). While PD-1 expression can indicate prior T cell activation and priming, it can also induce T cell exhaustion and dysfunction through binding to its ligand PD-L1 (Sharpe and Pauken, 2018; Sun et al., 2018). Indeed, immune, endothelial, and tumor cells each showed a significant increase in surface expression of PD-L1 after T/P treatment (Figure 5G). Therefore, despite initial influx of activated T cells into PDAC undergoing therapy-induced senescence, CD8+ T cells rapidly become phenotypically exhausted and do not contribute to an anti-tumor response.

T Cell Exhaustion Is Reversed by PD-1 Blockade that Triggers Anti-tumor Immunity

Induction of the PD-1/PD-L1 inhibitory axis in T cell inflamed tumors following T/P treatment provides a clear rationale for combining senescence-inducing agents with PD-1 blockade. First, we examined activation and exhaustion marker expression on CD8+ T cells isolated from KPC^{mut} cell transplant tumors treated with T/P in combination with PD-1 blockade (T/P/PD-1). Remarkably, CD8+ T cells from T/P/PD-1-treated tumors displayed reduced expression of exhaustion markers and increased co-expression of activation markers CD69 and CD44 compared to T/P treatment alone (Figures 6A–6C). These T cells also displayed higher TNF-α, INF-γ, and granzyme B expression compared to those harvested from tumors following T/P or PD-1 treatment alone, further indicative of reversion of lymphocyte dysfunction (Figures 6D and 6E).

Tumors isolated from mice treated with T/P and PD-1 blockade displayed increased apoptosis compared to anti-PD-1 therapy alone (Figure 6F). Activated T cells appeared to preferentially target senescent tumor cells, as T/P/PD-1-treated tumors showed a reduction in SA-β-gal positive cells compared to T/P treatment (Figure 6G). Both senescence-associated vascular remodeling and CD8+ T cell mobilization were required for these effects, because apoptosis produced by T/P/PD-1 treatment was abrogated by tumor specific suppression of p65, VEGFR-2 signaling disruption, VCAM-1 neutralization, and CD8 depletion (Figures 6F and 6H). Thus, PD-1 checkpoint

---

Figure 4. The SASP Promotes T Cell Infiltration via Endothelial Activation

(A and B) IHC staining and quantification of intratumoral total (A) and CD8+ (B) T cells per field in KPC^{flox} GEMM tumors treated with vehicle or trametinib (1 mg/kg) and palbociclib (100 mg/kg) for 2 weeks (n = 3; p < 0.01).

(C and D) Flow cytometry analysis of CD4+ (C) and CD8+ (D) T cells in KPC^{mut} cell transplant tumors following 2-week treatment with vehicle, trametinib (1 mg/kg), and/or palbociclib (100 mg/kg) (n = 5).

(E) Flow cytometry analysis of CD8+ T cells in KPC^{mut} cell transplant tumors harboring control Ren or p65 shRNAs and treated as in (A) (n = 4–7).

(F) Flow cytometry analysis of CD8+ T cells in KPC^{mut} cell transplant tumors treated with vehicle, trametinib (1 mg/kg), palbociclib (100 mg/kg), and/or a VEGFR-2 blocking antibody (DC101; 800 μg) for 2 weeks (n = 3–5).

(G) IHC staining and quantification of intratumoral T cells per field in KPC^{mut} organoid tumors harboring Ren or p65 shRNAs and treated as in (A) (n = 2–3; Ren T/P versus p65 T/P, p = 0.0001).

(H) IHC staining and quantification of intratumoral T cells per field in KPC^{flox} GEMM tumors treated as in (F) (n = 2–3; T/P versus T/P/DC101, p = 0.007).

(I) Flow cytometry analysis of CD8+ T cells in KPC^{mut} cell transplant tumors following 2-week treatment with vehicle, trametinib (1 mg/kg), palbociclib (100 mg/kg), and/or neutralizing mAbs targeting PSGL-1 (4RA10; 50 μg), ICAM-1 (YN1/1.7.4; 200 μg), or VCAM-1 (M/K-2.7; 200 μg) (n = 4–5).

(J) IHC staining and quantification of intratumoral T cells per field in KPC^{flox} GEMM tumors treated with vehicle, trametinib (1 mg/kg), palbociclib (100 mg/kg), and/or a VCAM-1 neutralizing antibody (M/K-2.7; 200 μg) for 2 weeks (n ≥ 3; T/P versus T/P/VCAM-1, p = 0.008). Values for V and T/P-treated cohorts are the same displayed in (A).

One-way ANOVA (C–F and I). Error bars, mean ± SEM. ****p < 0.001, ***p < 0.01, *p < 0.05. n.s., not significant. Scale bars, 50 μm.

See also Figure S5.
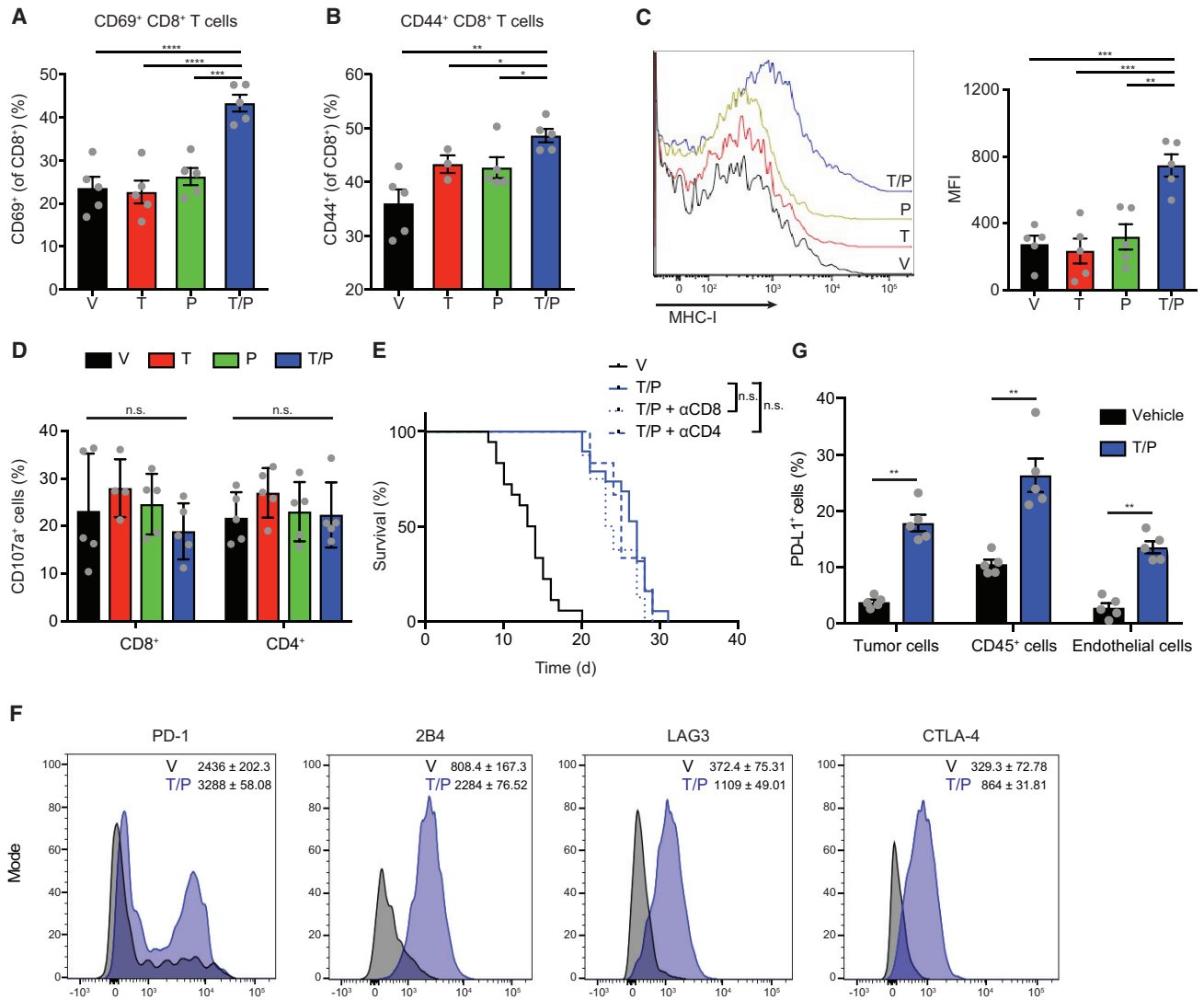
Figure 5. Therapy-Induced Senescence Leads to T Cell Activation and Exhaustion

(A–D) Flow cytometry analysis of KPC^{mut} cell transplant tumors following 2-week treatment with vehicle, trametinib (1 mg/kg) and/or palbociclib (100 mg/kg) (n = 3–5). (A) Percentage of CD69+ CD8+ T cells. (B) Percentage of CD44+ CD8+ T cells. (C) Representative histograms (left) and quantification of mean fluorescent intensity (MFI) of MHC-I (H-2k^b) expression on tumor cells. (D) Percentage of CD107a+ T cells.

(E) Kaplan-Meier survival curve of KPC^{mut} cell transplant mice treated with vehicle or trametinib (1 mg/kg) and palbociclib (100 mg/kg) in the presence or absence of a CD8 (2.43; 200 μg) or CD4 (GK1.5; 200 μg) depleting antibody (n ≥ 6).

(F and G) Flow cytometry analysis of KPC^{mut} cell transplant tumors following treatment as in (A). (F) Representative flow cytometry plots and MFI for PD-1 (p = 0.016), 2B4 (p < 0.0001), LAG3 (p < 0.0001), and CTLA-4 (p = 0.0002) expression on CD8+ T cells (n = 3–5). (G) Percentage of PD-L1+ tumor, immune, and endothelial cells (n = 5).

One-way ANOVA (A–D). Log-rank test (E). Error bars, mean ± SEM. ****p < 0.0001, ***p < 0.001, **p < 0.01, *p < 0.05. n.s., not significant.

See also Figure S6.

blockade reawakens exhausted CD8+ T cells to trigger antitumor immunity following senescence induction.

Senescence-Associated Vascular Remodeling Potentiates Immune Checkpoint Blockade

The above results prompted us to assess the efficacy of T/P/PD-1 therapy in our preclinical murine PDAC models. Studies suggest that immune checkpoint blockade efficacy is partly dependent on mutations recognized as "non-self" by T cells (Samstein et al., 2019; Schumacher and Schreiber, 2015); accordingly, we observed a mutation burden consistent with that of human PDAC in our mouse models (Figure S7A). Thus, PDAC-bearing KPC^{mut} organoid transplant or KPC^{flox} GEMM mice were treated with T/P and/or anti-PD-1 therapy and monitored for changes in biological responses, tumor growth, and overall survival.
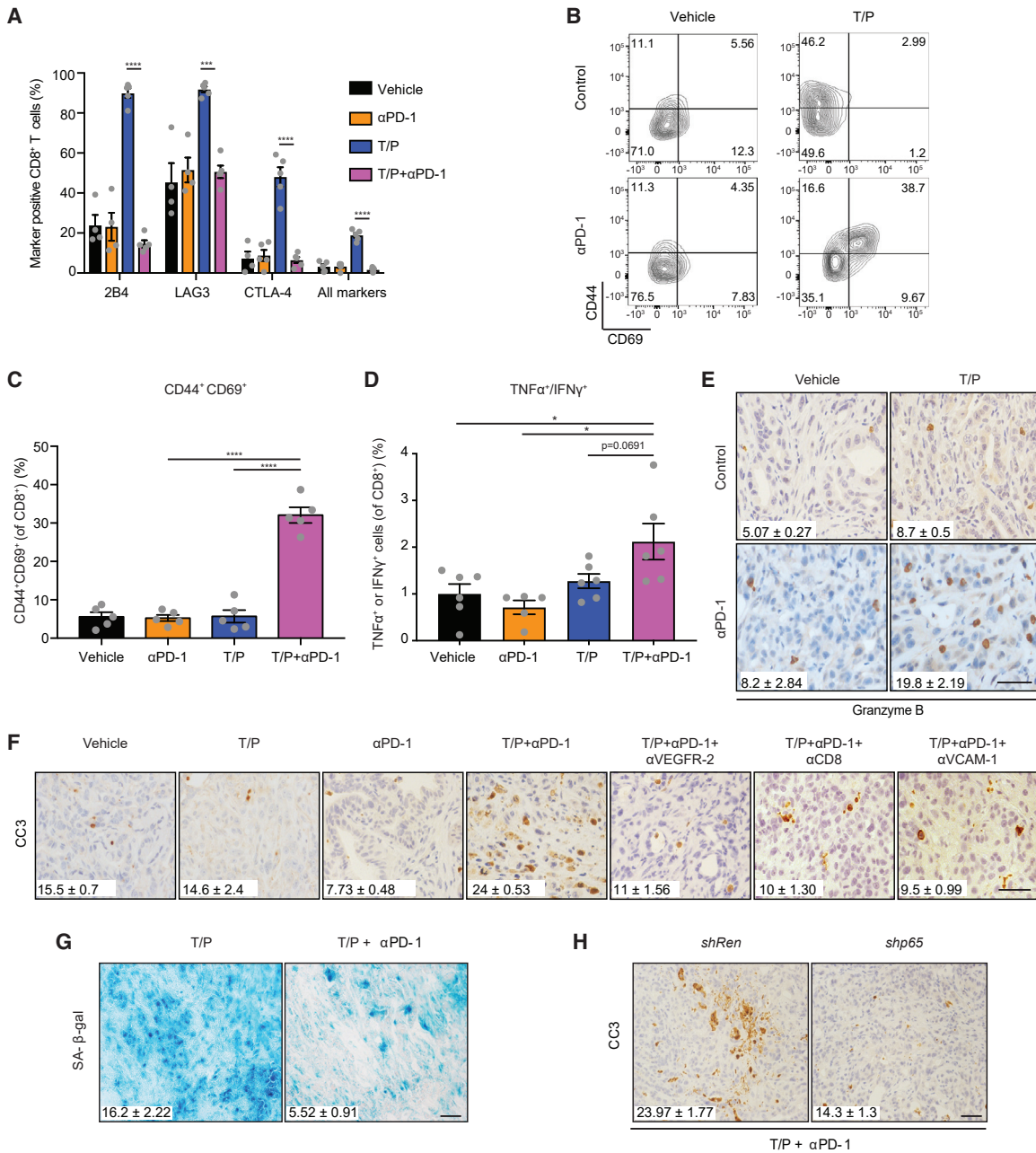
Figure 6. T Cell Exhaustion Is Reversed by PD-1 Blockade that Triggers Anti-tumor Immunity

(A–D) Flow cytometry analysis of KPC^{mut} cell transplant tumors following 2-week treatment with vehicle, trametinib (1 mg/kg), palbociclib (100 mg/kg), and/or a PD-1 blocking antibody (RMP1-14; 200 μg). (A) Exhaustion marker expression on CD8$^+$ T cells (n = 4–5). Representative flow cytometry plots (B) and quantification (C) of CD69 and CD44 expression on CD8$^+$ T cells (n = 5). (D) Percentage of CD8$^+$ T cells expressing TNF-α and/or IFN-γ (n = 5–6).

(E) IHC staining and quantification of granzyme B$^+$ cells in KPC^{mut} organoid transplant tumors following treatment as in (A) (n = 2–3; T/P versus T/P/PD-1, p = 0.030; PD-1 versus T/P/PD-1, p = 0.041).

(F) IHC staining and quantification of CC3$^+$ cells in KPC^{flox} GEMM tumors treated for 2 weeks with vehicle, trametinib (1 mg/kg), palbociclib (100 mg/kg), and/or mAbs targeting PD-1 (RMP1-14; 200 μg), VEGFR-2 (DC101; 800 μg), CD8 (2.43; 200 μg), or VCAM-1 (M/K-2.7; 200 μg) (n = 2-3; T/P versus T/P/PD-1, p = 0.016; T/P/PD-1 versus T/P/PD-1/DC101, p = 0.001; T/P/PD-1 versus T/P/PD-1/CD8, p = 0.0001; T/P/PD-1 versus T/P/PD-1/VCAM-1, p = 0.005). Values for V and T/P-treated cohorts are the same displayed in Figure 3G.

(G) Staining and quantification of SA-β-gal$^+$ area in KPC^{mut} organoid transplant tumors treated with trametinib (1 mg/kg) and palbociclib (100 mg/kg) in the presence or absence of a PD-1 blocking antibody (RMP1-14; 200 μg) for 2 weeks (n = 3; p = 0.011).

(H) KPC^{mut} organoid transplant tumors harboring *Ren* or *p65* shRNAs were treated for 2 weeks as in (G). Quantification of CC3$^+$ cells is shown (n = 3; p = 0.03).

One-way ANOVA (C and D). Error bars, mean ± SEM. ****p < 0.0001, ***p < 0.001, *p < 0.05. Scale bars, 50 μm.
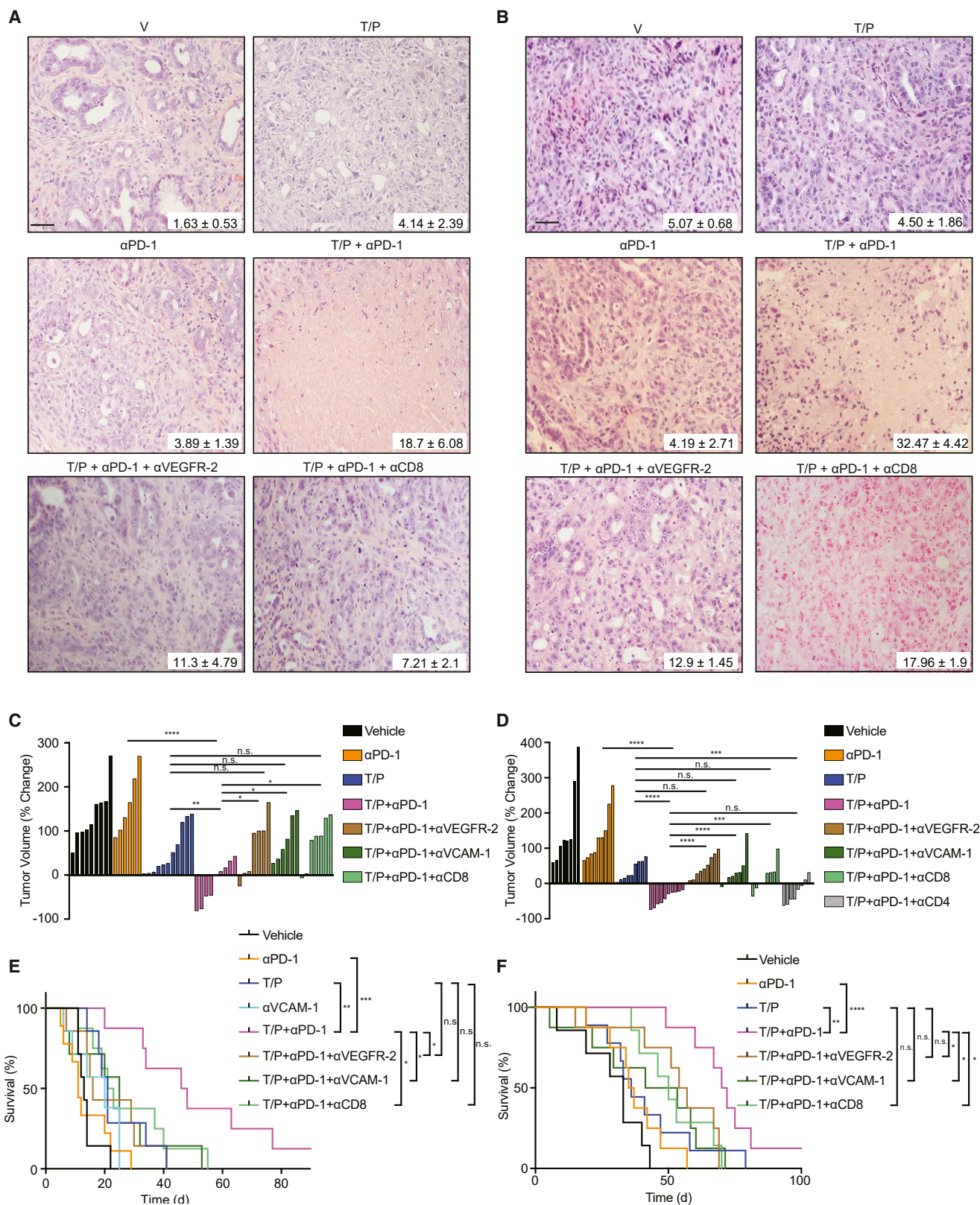
The anti-tumor effects of combining immune checkpoint blockade with the senescence-inducing T/P regimen went well beyond what was observed following standard-of-care gemcitabine (see Figure 3), or either T/P or anti-PD1 treatment alone. Two-week treatment with T/P/PD-1 produced areas of tumor destruction visible by gross histology and tumor regressions in 4/9 *KPC^flox* GEMM and 10/10 *KPC^mut* organoid transplant mice (Figures 7A–7D). By contrast, all tumors treated with anti-PD1 alone continued to progress after 2-week treatment (Figures 7C and 7D). These anti-tumor effects translated into increased survival, producing an over 5-fold increase in the median survival of *KPC^flox* GEMM mice treated with T/P/PD-1 as compared to PD-1 alone and a number of long-term survivors in both models (Figures 7E and 7F). The anti-tumor effects of PD-1 checkpoint blockade were predicated on potent MEK inhibition, as administration of the T/P/PD-1 regimen at a suboptimal trametinib dose (0.3 mg/kg) that was insufficient to inhibit ERK phosphorylation or induce senescence and its vascular or T cell remodeling effects was not efficacious (Figures S7B–S7D). These data imply that senescence induction upon combined T/P treatment is necessary to potentiate PD-1 blockade in PDAC models.

We also evaluated treatment responses in PDAC-bearing mice in which SASP was disabled by *p65* shRNA, vascular remodeling was perturbed by VEGFR-2 or VCAM-1 antibodies, or either CD4+ or CD8+ T cells were depleted. *p65*, VEGFR-2, or VCAM-1 inhibition largely blocked the ability of T/P/PD-1 treatment to elicit tumor destruction and produce robust tumor regressions (Figures 7A–7F, S7E, and S7F). Synergy between T/P treatment and PD-1 blockade was dependent on CD8+, but not CD4+ T cells (Figures 7A–7F). Histological analysis of *KPC^flox* GEMM tumors that relapsed after long-term T/P/PD-1 therapy consistently showed hypovascularization, as well as poor endothelial activation and T cell penetration, similar to those of vehicle-treated mice (Figures S7G–S7I). These data imply that senescence-inducing therapies can increase T cell infiltration and reactivity in previously immunologically "cold" tumors, thus sensitizing PDAC to immune checkpoint blockade.

DISCUSSION

The desmoplastic stroma of PDAC fosters a hypovascularized and immune suppressive TME that impedes the penetration of small molecule drugs and stifles anti-tumor immunity, leading to *de novo* resistance to chemotherapy and immune checkpoint blockade (Brahmer et al., 2012; Carmichael et al., 1996; Olive et al., 2009; Royal et al., 2010). Here, we show how molecularly targeted therapies that drive PDAC cells into senescence can engage a tumor suppressive program that remodels the TME and creates therapeutic vulnerabilities, at least in part, through SASP-facilitated vascular remodeling. On one hand, this response increases blood vessel density and permeability, leading to enhanced uptake and activity of the chemotherapeutic drug gemcitabine; on the other, it facilitates the tumor infiltration of CD8+ T cells that, although exhausted, can be reawakened by checkpoint blockade. As a consequence, the addition of gemcitabine or anti-PD-1 therapy to the T/P regimen produces tumor cell death and sustained tumor regressions in otherwise highly refractory PDAC models.

The impact of therapy-induced senescence on PDAC vasculature function was unexpected. While the SASP can alter endothelial cell behavior in culture and in xenograft models, the biological impact of pro-angiogenic SASP factors on the TME has been hypothesized to be pro-oncogenic (Ancrile et al., 2007; Coppé et al., 2006; Mikuła-Pietrasik et al., 2016; Oubaha et al., 2016). However, in PDAC, these SASP factors produce the opposite outcome, leading to improved access of small molecules and immune cells into the tumor that ultimately enables its destruction. Mechanistically, SASP-facilitated vascular remodeling involves collaboration between pro-angiogenic (e.g., VEGF) and pro-inflammatory (e.g., CCL5, CXCL-1, and IL-6) SASP components, leading to increased blood vessel density and endothelial cell activation, respectively. While stromal sources of angiogenic or inflammatory cytokines may potentiate its effects, our results demonstrate that SASP secretion from tumor cells is essential for the observed phenotypes.

Neo-angiogenesis is typically considered a prerequisite for cancer progression and, as such, therapies that inhibit this process have been a focus of drug development efforts (Hanahan and Weinberg, 2000; Jain et al., 2006; Zirlik and Duyster, 2018). By contrast, owing to the hypovascularity of PDAC, studies suggest that therapies that improve, rather than inhibit, vascular function might establish therapeutic windows for treating this disease (Olive et al., 2009; Provenzano et al., 2012). One such approach involves disrupting stromal hedgehog signaling, which leads to increased vascular perfusion and drug accessibility by inhibiting myofibroblast activity (Olive et al., 2009). Yet, over time, depletion of key tumor suppressive stromal elements with this method culminates in tumor cell

---

Figure 7. Senescence-Associated Vascular Remodeling Potentiates Immune Checkpoint Blockade in PDAC

(A) H&E staining of *KPC^flox* GEMM tumors treated for 2 weeks with vehicle, trametinib (1 mg/kg), palbociclib (100 mg/kg), and/or mAbs targeting PD-1 (RMP1-14; 200 µg), VEGFR-2 (DC101; 800 µg), or CD8 (2.43; 200 µg). Percent of tumor covered in necrosis is shown (n = 3; T/P versus T/P/PD-1, p = 0.08; PD-1 versus T/P/PD-1, p = 0.027).

(B) H&E staining of *KPC^mut* organoid transplant tumors treated for 2 weeks as in (A). Percent of tumor covered in necrosis is shown (n = 3; T/P versus T/P/PD-1, p = 0.004; PD-1 versus T/P/PD-1, p = 0.019; T/P/PD-1 versus T/P/PD-1/DC101, p = 0.016; T/P/PD-1 versus T/P/PD-1/CD8, p = 0.09).

(C and D) Waterfall plot of the response of *KPC^flox* GEMM (C) and *KPC^mut* organoid transplant (D) tumors after 2 weeks of treatment with vehicle, trametinib (1 mg/kg), palbociclib (100 mg/kg), and/or mAbs targeting PD-1 (RMP1-14; 200 µg), VEGFR-2 (DC101; 800 µg), CD8 (2.43; 200 µg), CD4 (GK1.5; 200 µg), or VCAM-1 (M/K-2.7; 200 µg) (n ≥ 6). Values for V and T/P-treated cohorts are the same displayed in Figures 3C and 3E.

(E and F) Kaplan-Meier survival curves of *KPC^flox* GEMM (E) and *KPC^mut* organoid transplant (F) mice treated as in (D) (n ≥ 7). Values for V and T/P-treated cohorts are the same displayed in Figures 3D and 3F.

One-way ANOVA (C and D). Log-rank test (E and F). Error bars, mean ± SEM. ****p < 0.0001, ***p < 0.001, **p < 0.01, *p < 0.05. n.s., not significant. Scale bars, 50 µm.

See also Figure S7.

dedifferentiation and a more aggressive and metastatic disease (Rhim et al., 2014; Rosow et al., 2012). By contrast, the manner in which therapy-induced senescence increases tumor perfusion is distinct, producing a more functional vasculature without compromising tumor suppressive stromal components or promoting metastasis. Additionally, T/P-induced reduction in stromal HA content may relieve interstitial fluid pressures and contribute to enhanced vascular perfusion in our models (Provenzano et al., 2012).

Despite its limited activity, gemcitabine is part of the standard-of-care therapy for pancreatic cancer patients. While combinatorial approaches using gemcitabine are in pre-clinical and clinical use, the notion of combining cytostatic therapies with gemcitabine would not typically be pursued owing to the apparent requirement for DNA synthesis for gemcitabine-mediated toxicity (Plunkett et al., 1995). Yet, our data demonstrate that T/P therapy facilitates both gemcitabine uptake and its ability to promote tumor cell apoptosis, similar to what occurs following treatment with other agents that increase vascular perfusion in PDAC (Olive et al., 2009; Provenzano et al., 2012). We suspect that the efficacy of this three-drug combination is not a result of tumor-cell specific synergies, but instead arises from the improved ability of gemcitabine to target tumor cells that fail to senesce upon T/P treatment. Still, it remains possible that genomic instability resulting from senescence induction (Kotsantis et al., 2018; Woo and Poon, 2004), perhaps exacerbated by a defective p53-dependent G1 checkpoint, might also enhance gemcitabine cytotoxicity.

In addition to promoting uptake of soluble factors, SASP-facilitated vascular remodeling enables T cell penetration into PDAC and improves the efficacy of checkpoint blockade. Here, one critical outcome of SASP induction is increased endothelial cell expression of VCAM-1, a cell surface protein that stimulates lymphocyte adhesion and extravasation into tissues. Indeed, VCAM-1 is required for T cell infiltration and potentiation of PD-1 blockade following T/P therapy in our PDAC models. Collectively, these observations provide a compelling link between therapy-induced SASP, vascular remodeling, and immune cell infiltration, and add to a growing body of evidence that vascular normalization can enhance the efficacy of other T cell-directed immunotherapies (Buckanovich et al., 2008; Hamzah et al., 2008; Huang et al., 2012; Shrimali et al., 2010).

Previous work has established that targeted therapies, including CDK4/6 inhibitors, can cooperate with PD-1/PD-L1 blockade in other cancers (Deng et al., 2018; Ebert et al., 2016; Goel et al., 2017; Schaer et al., 2018). However, in contrast to our work, these studies employed immunologically "hot" and T cell "rich" cancer models that are typically responsive to checkpoint blockade. Moreover, focus of previous work has been on how these agents might increase T cell recognition or cytotoxicity rather than how T cells gain access to the tumor. Our study uses immunologically "cold" models of PDAC, a disease unresponsive to checkpoint blockade, to establish a mechanism for the latter effect, showing how T/P-induced senescence leads to endothelial activation and VCAM-1 upregulation that promotes T cell extravasation into tumors and sets the stage for efficient immunotherapy responses. Tumor cell autonomous effects may also play a role in stimulating T cell reactivity, and it is

noteworthy that MHC-I upregulation following T/P treatment of PDAC cells is much greater than that produced by either agent alone.

The effects of the SASP on the TME can be context-dependent. Thus, while the most prominent effects of T/P therapy in PDAC are SASP-dependent vascular remodeling and T cell surveillance, the outcome of T/P-induced senescence in lung cancer models involves a SASP-facilitated NK cell surveillance program (Ruscetti et al., 2018). This tissue specificity cannot be explained by differences in tumor genotype (both studies used models driven by mutant KRAS and p53 alterations) or in VEGF secretion (that was induced in pancreas and lung cancer models). Instead, we hypothesize that these contextual differences arise from the tissue architecture of tumors arising in each organ: the lungs are generally NK cell-rich and lung tumors are highly vascularized; by contrast, the pancreas harbors few NK cells and PDAC tumors are avascular (Salmon et al., 2019). As such, each TME may be more or less susceptible to different SASP components. Regardless, in both models, pharmacological induction of senescence can evoke latent anti-tumor immunity.

We suspect the profound tissue remodeling observed following therapy-induced senescence reflects the reengagement of an innate tumor suppressive mechanism that participates in tissue regeneration. Numerous studies suggest that senescence coordinates tissue remodeling activities associated with wound repair and resolution that are critical for organ homeostasis (Demaria et al., 2014; Krizhanovsky et al., 2008; Lujambio et al., 2013; Mosteiro et al., 2016; Neves et al., 2015). In the presence of chronic tissue damage, hyperactivation of this wound-healing response without senescent cell clearance can be deleterious and even pro-oncogenic (Baker et al., 2016; Demaria et al., 2017; Schafer et al., 2017). However, when acutely activated in tumor cells, the senescence program recapitulates many aspects of this native wound resolution response, halting further tumor cell proliferation while simultaneously modulating multiple components of the tissue environment to promote homeostasis. As such, senescence induction may prove more effective at remodeling the TME than targeting individual tissue components. It will be interesting to compare and contrast the immune-enhancing effects of senescence-inducing therapies to agents that target specific immune suppressive factors in PDAC (Feig et al., 2013; Jiang et al., 2016; Panni et al., 2019).

Our data provide a clear rationale for combining senescence-inducing therapies with both chemotherapy and immunotherapy to cull heterogeneous tumor cell populations in PDAC and perhaps other cancers as well. Although well-tolerated in our mouse models, the potential toxicities of the three drug combinations (trametinib and palbociclib together with either gemcitabine or anti-PD-1) will need to be closely monitored when extending these preclinical findings to human clinical trials. In principle, the stability of the senescence phenotype following T/P treatment may enable treatment regimens where these agents can be given sequentially on alternating schedules instead of simultaneously and continuously. It is noteworthy that treatment of BRAF mutant melanoma patients with a combination of MEK and BRAF inhibitors together with PD-1 blockade is highly efficacious and can be tolerated using an appropriate

regimen (Ribas et al., 2019). While the MEK and CDK4/6 inhibitor combination studied herein is a potent inducer of senescence in KRAS mutant cancers, other targeted and cytotoxic agents can also promote tumor cell senescence across a spectrum of cancer lineages and genotypic contexts (Ewald et al., 2010; Sieben et al., 2018). Consequently, our study provides one paradigm for combining such agents with immunomodulatory therapies to improve therapeutic outcomes.

STAR★METHODS

Detailed methods are provided in the online version of this paper and include the following:

- KEY RESOURCES TABLE
- LEAD CONTACT AND MATERIALS AVAILABILITY
- EXPERIMENTAL MODEL AND SUBJECT DETAILS
  - Cell and organoid culture and derivation
  - Animal Studies
- METHOD DETAILS
  - Compounds
  - Short-hairpin RNA (shRNA) knockdown
  - Preclinical drug studies
  - Neutralizing antibody studies
  - Ultrasound Imaging
  - Bioluminescence imaging
  - Tumor perfusion, permeability, and drug uptake assays
  - Flow cytometry
  - *In vivo* degranulation assay
  - Immunohistochemistry and immunofluorescence
  - SA-β-gal staining
  - Conditioned Media collection
  - Cytokine array
  - *In vitro* cell growth assays
  - *In vitro* endothelial tube formation assay
  - T cell functionality assays
  - qRT-PCR
  - High throughput RNA-sequencing (RNA-seq) analysis
  - Clustering and Gene Set Enrichment Analysis (GSEA)
  - Whole exome sequencing (WES)
- QUANTIFICATION AND STATISTICAL ANALYSIS
  - Histological and Image Analysis
  - Statistical analysis
- DATA AND CODE AVAILABILITY

SUPPLEMENTAL INFORMATION

Supplemental Information can be found online at https://doi.org/10.1016/j.cell.2020.03.008.

AUTHOR CONTRIBUTIONS

M.R., J.P.M., and R.M. conceived the project, performed and analyzed experiments, and wrote the paper with assistance from all authors. M.F., D.A.-C., R.S., and D.A.H. performed and analyzed experiments. J.R., J. Leibold, P.B.R., J.S. A.K., J. Li, R.J.N., E.d.S., and B.Z.S. provided animal models and performed and analyzed *in vivo* experiments. Y.-j.H. analyzed genomic and transcriptomic datasets. J.E.W. provided histopathological analysis of tissue specimens. C.J.S. and S.W.L. conceived the project, supervised experiments, and wrote the paper.

DECLARATION OF INTERESTS

P.B.R. is a consultant for EMD Serono. D.A.H. is a cofounder of LipidSense, Inc., a cofounder and officer with equity interest in Goldilocks Therapeutics Inc., and a member of the scientific advisory board of Concarlo Holdings, LLC. B.Z.S. is an advisor to iTeos Therapeutics and receives research funding from Boehringer Ingelheim. S.W.L. is a founder and scientific advisory board member of Blueprint Medicines, ORIC Pharmaceuticals, and Geras Bio and received an award and honorarium from Eli Lilly and Company. M.R., J.P.M., R.M., J. Leibold, C.J.S., and S.W.L. have filed a U.S. patent application (Ser. No. 62/694,519) related to this work.

REFERENCES

Alexandrov, L.B., Nik-Zainal, S., Wedge, D.C., Aparicio, S.A., Behjati, S., Biankin, A.V., Bignell, G.R., Bolli, N., Borg, A., Børresen-Dale, A.L., et al.; Australian Pancreatic Cancer Genome Initiative; ICGC Breast Cancer Consortium; ICGC MMML-Seq Consortium; ICGC PedBrain (2013). Signatures of mutational processes in human cancer. Nature *500*, 415–421.

Ancrile, B., Lim, K.H., and Counter, C.M. (2007). Oncogenic Ras-induced secretion of IL6 is required for tumorigenesis. Genes Dev. *21*, 1714–1719.

Anders, S., Pyl, P.T., and Huber, W. (2015). HTSeq–a Python framework to work with high-throughput sequencing data. Bioinformatics *31*, 166–169.

Baker, D.J., Childs, B.G., Durik, M., Wijers, M.E., Sieben, C.J., Zhong, J., Saltness, R.A., Jeganathan, K.B., Verzosa, G.C., Pezeshki, A., et al. (2016). Naturally occurring p16(Ink4a)-positive cells shorten healthy lifespan. Nature *530*, 184–189.

Bardeesy, N., Aguirre, A.J., Chu, G.C., Cheng, K.H., Lopez, L.V., Hezel, A.F., Feng, B., Brennan, C., Weissleder, R., Mahmood, U., et al. (2006). Both p16(Ink4a) and the p19(Arf)-p53 pathway constrain progression of pancreatic adenocarcinoma in the mouse. Proc. Natl. Acad. Sci. USA *103*, 5947–5952.

Blando, J., Sharma, A., Higa, M.G., Zhao, H., Vence, L., Yadav, S.S., Kim, J., Sepulveda, A.M., Sharp, M., Maitra, A., et al. (2019). Comparison of immune infiltrates in melanoma and pancreatic cancer highlights VISTA as a potential target in pancreatic cancer. Proc. Natl. Acad. Sci. USA *116*, 1692–1697.

Boj, S.F., Hwang, C.I., Baker, L.A., Chio, I.I., Engle, D.D., Corbo, V., Jager, M., Ponz-Sarvise, M., Tiriac, H., Spector, M.S., et al. (2015). Organoid models of human and mouse ductal pancreatic cancer. Cell *160*, 324–338.

Bolger, A.M., Lohse, M., and Usadel, B. (2014). Trimmomatic: a flexible trimmer for Illumina sequence data. Bioinformatics *30*, 2114–2120.

Brahmer, J.R., Tykodi, S.S., Chow, L.Q., Hwu, W.J., Topalian, S.L., Hwu, P., Drake, C.G., Camacho, L.H., Kauh, J., Odunsi, K., et al. (2012). Safety and activity of anti-PD-L1 antibody in patients with advanced cancer. N. Engl. J. Med. *366*, 2455–2465.

Brea, E.J., Oh, C.Y., Manchado, E., Budhu, S., Gejman, R.S., Mo, G., Mondello, P., Han, J.E., Jarvis, C.A., Ulmert, D., et al. (2016). Kinase Regulation of Human MHC Class I Molecule Expression on Cancer Cells. Cancer Immunol. Res. *4*, 936–947.

Buckanovich, R.J., Facciabene, A., Kim, S., Benencia, F., Sasaroli, D., Balint, K., Katsaros, D., O'Brien-Jenkins, A., Gimotty, P.A., and Coukos, G. (2008). Endothelin B receptor mediates the endothelial barrier to T cell homing to tumors and disables immune therapy. Nat. Med. *14*, 28–36.

Caldwell, M.E., DeNicola, G.M., Martins, C.P., Jacobetz, M.A., Maitra, A., Hruban, R.H., and Tuveson, D.A. (2012). Cellular features of senescence during the evolution of human and murine ductal pancreatic cancer. Oncogene *31*, 1599–1608.

Carmichael, J., Fink, U., Russell, R.C., Spittle, M.F., Harris, A.L., Spiessi, G., and Blatter, J. (1996). Phase II study of gemcitabine in patients with advanced pancreatic cancer. Br. J. Cancer *73*, 101–105.

Carrière, C., Gore, A.J., Norris, A.M., Gunn, J.R., Young, A.L., Longnecker, D.S., and Korc, M. (2011). Deletion of Rb accelerates pancreatic carcinogenesis by oncogenic Kras and impairs senescence in premalignant lesions. Gastroenterology *141*, 1091–1101.

Chauhan, V.P., Martin, J.D., Liu, H., Lacorre, D.A., Jain, S.R., Kozin, S.V., Stylianopoulos, T., Mousa, A.S., Han, X., Adstamongkonkul, P., et al. (2013). Angiotensin inhibition enhances drug delivery and potentiates chemotherapy by decompressing tumour blood vessels. Nat. Commun. *4*, 2516.

Chicas, A., Wang, X., Zhang, C., McCurrach, M., Zhao, Z., Mert, O., Dickins, R.A., Narita, M., Zhang, M., and Lowe, S.W. (2010). Dissecting the unique role of the retinoblastoma tumor suppressor during cellular senescence. Cancer Cell *17*, 376–387.

Chien, Y., Scuoppo, C., Wang, X., Fang, X., Balgley, B., Bolden, J.E., Premsrirut, P., Luo, W., Chicas, A., Lee, C.S., et al. (2011). Control of the senescence-associated secretory phenotype by NF-κB promotes senescence and enhances chemosensitivity. Genes Dev. *25*, 2125–2136.

Cibulskis, K., Lawrence, M.S., Carter, S.L., Sivachenko, A., Jaffe, D., Sougnez, C., Gabriel, S., Meyerson, M., Lander, E.S., and Getz, G. (2013). Sensitive detection of somatic point mutations in impure and heterogeneous cancer samples. Nat. Biotechnol. *31*, 213–219.

Clark, C.E., Hingorani, S.R., Mick, R., Combs, C., Tuveson, D.A., and Vonderheide, R.H. (2007). Dynamics of the immune reaction to pancreatic cancer from inception to invasion. Cancer Res. *67*, 9518–9527.

Collins, M.A., Bednar, F., Zhang, Y., Brisset, J.C., Galbán, S., Galbán, C.J., Rakshit, S., Flannagan, K.S., Adsay, N.V., and Pasca di Magliano, M. (2012a). Oncogenic Kras is required for both the initiation and maintenance of pancreatic cancer in mice. J. Clin. Invest. *122*, 639–653.

Collins, M.A., Brisset, J.C., Zhang, Y., Bednar, F., Pierre, J., Heist, K.A., Galbán, C.J., Galbán, S., and di Magliano, M.P. (2012b). Metastatic pancreatic cancer is dependent on oncogenic Kras in mice. PLoS ONE *7*, e49707.

Coppé, J.P., Kauser, K., Campisi, J., and Beauséjour, C.M. (2006). Secretion of vascular endothelial growth factor by primary human fibroblasts at senescence. J. Biol. Chem. *281*, 29568–29574.

Coppé, J.P., Patil, C.K., Rodier, F., Sun, Y., Muñoz, D.P., Goldstein, J., Nelson, P.S., Desprez, P.Y., and Campisi, J. (2008). Senescence-associated secretory phenotypes reveal cell-nonautonomous functions of oncogenic RAS and the p53 tumor suppressor. PLoS Biol. *6*, 2853–2868.

Coppé, J.P., Desprez, P.Y., Krtolica, A., and Campisi, J. (2010). The senescence-associated secretory phenotype: the dark side of tumor suppression. Annu. Rev. Pathol. *5*, 99–118.

Demaria, M., Ohtani, N., Youssef, S.A., Rodier, F., Toussaint, W., Mitchell, J.R., Laberge, R.M., Vijg, J., Van Steeg, H., Dollé, M.E., et al. (2014). An essential role for senescent cells in optimal wound healing through secretion of PDGF-AA. Dev. Cell *31*, 722–733.

Demaria, M., O'Leary, M.N., Chang, J., Shao, L., Liu, S., Alimirah, F., Koenig, K., Le, C., Mitin, N., Deal, A.M., et al. (2017). Cellular Senescence Promotes Adverse Effects of Chemotherapy and Cancer Relapse. Cancer Discov. *7*, 165–176.

Deng, J., Wang, E.S., Jenkins, R.W., Li, S., Dries, R., Yates, K., Chhabra, S., Huang, W., Liu, H., Aref, A.R., et al. (2018). CDK4/6 Inhibition Augments Antitumor Immunity by Enhancing T-cell Activation. Cancer Discov. *8*, 216–233.

Dobin, A., Davis, C.A., Schlesinger, F., Drenkow, J., Zaleski, C., Jha, S., Batut, P., Chaisson, M., and Gingeras, T.R. (2013). STAR: ultrafast universal RNA-seq aligner. Bioinformatics *29*, 15–21.

Ebert, P.J.R., Cheung, J., Yang, Y., McNamara, E., Hong, R., Moskalenko, M., Gould, S.E., Maecker, H., Irving, B.A., Kim, J.M., et al. (2016). MAP Kinase Inhibition Promotes T Cell and Anti-tumor Activity in Combination with PD-L1 Checkpoint Blockade. Immunity *44*, 609–621.

Ewald, J.A., Desotelle, J.A., Wilding, G., and Jarrard, D.F. (2010). Therapy-induced senescence in cancer. J. Natl. Cancer Inst. *102*, 1536–1546.

Faget, D.V., Ren, Q., and Stewart, S.A. (2019). Unmasking senescence: context-dependent effects of SASP in cancer. Nat. Rev. Cancer *19*, 439–453.

Feig, C., Jones, J.O., Kraman, M., Wells, R.J., Deonarine, A., Chan, D.S., Connell, C.M., Roberts, E.W., Zhao, Q., Caballero, O.L., et al. (2013). Targeting CXCL12 from FAP-expressing carcinoma-associated fibroblasts synergizes with anti-PD-L1 immunotherapy in pancreatic cancer. Proc. Natl. Acad. Sci. USA *110*, 20212–20217.

Goel, S., DeCristo, M.J., Watt, A.C., BrinJones, H., Sceneay, J., Li, B.B., Khan, N., Ubellacker, J.M., Xie, S., Metzger-Filho, O., et al. (2017). CDK4/6 inhibition triggers anti-tumour immunity. Nature *548*, 471–475.

Hamzah, J., Jugold, M., Kiessling, F., Rigby, P., Manzur, M., Marti, H.H., Rabie, T., Kaden, S., Gröne, H.J., Hämmerling, G.J., et al. (2008). Vascular normalization in Rgs5-deficient tumours promotes immune destruction. Nature *453*, 410–414.

Hanahan, D., and Weinberg, R.A. (2000). The hallmarks of cancer. Cell *100*, 57–70.

Herreros-Villanueva, M., Hijona, E., Cosme, A., and Bujanda, L. (2012). Mouse models of pancreatic cancer. World J. Gastroenterol. *18*, 1286–1294.

Hingorani, S.R., Petricoin, E.F., Maitra, A., Rajapakse, V., King, C., Jacobetz, M.A., Ross, S., Conrads, T.P., Veenstra, T.D., Hitt, B.A., et al. (2003). Preinvasive and invasive ductal pancreatic cancer and its early detection in the mouse. Cancer Cell *4*, 437–450.

Huang, Y., Yuan, J., Righi, E., Kamoun, W.S., Ancukiewicz, M., Nezivar, J., Santosuosso, M., Martin, J.D., Martin, M.R., Vianello, F., et al. (2012). Vascular normalizing doses of antiangiogenic treatment reprogram the immunosuppressive tumor microenvironment and enhance immunotherapy. Proc. Natl. Acad. Sci. USA *109*, 17561–17566.

Huang, Y., Kim, B.Y.S., Chan, C.K., Hahn, S.M., Weissman, I.L., and Jiang, W. (2018). Improving immune-vascular crosstalk for cancer immunotherapy. Nat. Rev. Immunol. *18*, 195–203.

Hunt, B.J., and Jurd, K.M. (1998). Endothelial cell activation. A central pathophysiological process. BMJ *316*, 1328–1329.

Jain, R.K., Duda, D.G., Clark, J.W., and Loeffler, J.S. (2006). Lessons from phase III clinical trials on anti-VEGF therapy for cancer. Nat. Clin. Pract. Oncol. 3, 24–40.

Jiang, H., Hegde, S., Knolhoff, B.L., Zhu, Y., Herndon, J.M., Meyer, M.A., Nywening, T.M., Hawkins, W.G., Shapiro, I.M., Weaver, D.T., et al. (2016). Targeting focal adhesion kinase renders pancreatic cancers responsive to checkpoint immunotherapy. Nat. Med. 22, 851–860.

Kang, T.W., Yevsa, T., Woller, N., Hoenicke, L., Wuestefeld, T., Dauch, D., Hohmeyer, A., Gereke, M., Rudalska, R., Potapova, A., et al. (2011). Senescence surveillance of pre-malignant hepatocytes limits liver cancer development. Nature 479, 547–551.

Kapoor, A., Yao, W., Ying, H., Hua, S., Liewen, A., Wang, Q., Zhong, Y., Wu, C.J., Sadanandam, A., Hu, B., et al. (2014). Yap1 activation enables bypass of oncogenic Kras addiction in pancreatic cancer. Cell 158, 185–197.

Kotsantis, P., Petermann, E., and Boulton, S.J. (2018). Mechanisms of Oncogene-Induced Replication Stress: Jigsaw Falling into Place. Cancer Discov. 8, 537–555.

Kraman, M., Bambrough, P.J., Arnold, J.N., Roberts, E.W., Magiera, L., Jones, J.O., Gopinathan, A., Tuveson, D.A., and Fearon, D.T. (2010). Suppression of antitumor immunity by stromal cells expressing fibroblast activation protein-alpha. Science 330, 827–830.

Krizhanovsky, V., Yon, M., Dickins, R.A., Hearn, S., Simon, J., Miething, C., Yee, H., Zender, L., and Lowe, S.W. (2008). Senescence of activated stellate cells limits liver fibrosis. Cell 134, 657–667.

Kuilman, T., and Peeper, D.S. (2009). Senescence-messaging secretome: SMS-ing cellular stress. Nat. Rev. Cancer 9, 81–94.

Kuleshov, M.V., Jones, M.R., Rouillard, A.D., Fernandez, N.F., Duan, Q., Wang, Z., Koplev, S., Jenkins, S.L., Jagodnik, K.M., Lachmann, A., et al. (2016). Enrichr: a comprehensive gene set enrichment analysis web server 2016 update. Nucleic Acids Res. 44 (W1), W90-7.

Lee, J.J., Perera, R.M., Wang, H., Wu, D.C., Liu, X.S., Han, S., Fitamant, J., Jones, P.D., Ghanta, K.S., Kawano, S., et al. (2014). Stromal response to Hedgehog signaling restrains pancreatic cancer progression. Proc Natl Acad Sci U S A, E3091–E3100.

Lesina, M., Wörmann, S.M., Morton, J., Diakopoulos, K.N., Korneeva, O., Wimmer, M., Einwächter, H., Sperveslage, J., Demir, I.E., Kehl, T., et al. (2016). RelA regulates CXCL1/CXCR2-dependent oncogene-induced senescence in murine Kras-driven pancreatic carcinogenesis. J. Clin. Invest. 126, 2919–2932.

Li, H., and Durbin, R. (2009). Fast and accurate short read alignment with Burrows-Wheeler transform. Bioinformatics 25, 1754–1760.

Liao, Y., Smyth, G.K., and Shi, W. (2014). featureCounts: an efficient general purpose program for assigning sequence reads to genomic features. Bioinformatics 30, 923–930.

Ligorio, M., Sil, S., Malagon-Lopez, J., Nieman, L.T., Misale, S., Di Pilato, M., Ebright, R.Y., Karabacak, M.N., Kulkarni, A.S., Liu, A., et al. (2019). Stromal Microenvironment Shapes the Intratumoral Architecture of Pancreatic Cancer. Cell 178, 160–175 e127.

Lorenzon, P., Vecile, E., Nardon, E., Ferrero, E., Harlan, J.M., Tedesco, F., and Dobrina, A. (1998). Endothelial cell E- and P-selectin and vascular cell adhesion molecule-1 function as signaling receptors. J. Cell Biol. 142, 1381–1391.

Love, M.I., Huber, W., and Anders, S. (2014). Moderated estimation of fold change and dispersion for RNA-seq data with DESeq2. Genome Biol. 15, 550.

Lujambio, A., Akkari, L., Simon, J., Grace, D., Tschaharganeh, D.F., Bolden, J.E., Zhao, Z., Thapar, V., Joyce, J.A., Krizhanovsky, V., and Lowe, S.W. (2013). Non-cell-autonomous tumor suppression by p53. Cell 153, 449–460.

Manchado, E., Weissmueller, S., Morris, J.P., 4th, Chen, C.C., Wullenkord, R., Lujambio, A., de Stanchina, E., Poirier, J.T., Gainor, J.F., Corcoran, R.B., et al. (2016). A combinatorial strategy for treating KRAS-mutant lung cancer. Nature 534, 647–651.

Martin, M. (2011). Cutadapt removes adapter sequences from high-throughput sequencing reads. EMBnet.journal 17, 10–12.

McKenna, A., Hanna, M., Banks, E., Sivachenko, A., Cibulskis, K., Kernytsky, A., Garimella, K., Altshuler, D., Gabriel, S., Daly, M., and DePristo, M.A. (2010). The Genome Analysis Toolkit: a MapReduce framework for analyzing next-generation DNA sequencing data. Genome Res. 20, 1297–1303.

Meylan, E., Dooley, A.L., Feldser, D.M., Shen, L., Turk, E., Ouyang, C., and Jacks, T. (2009). Requirement for NF-kappaB signalling in a mouse model of lung adenocarcinoma. Nature 462, 104–107.

Mikuła-Pietrasik, J., Sosińska, P., Naumowicz, E., Maksin, K., Piotrowska, H., Woźniak, A., Szpurek, D., and Książek, K. (2016). Senescent peritoneal mesothelium induces a pro-angiogenic phenotype in ovarian cancer cells in vitro and in a mouse xenograft model in vivo. Clin. Exp. Metastasis 33, 15–27.

Morris, J.P., 4th, Wang, S.C., and Hebrok, M. (2010). KRAS, Hedgehog, Wnt and the twisted developmental biology of pancreatic ductal adenocarcinoma. Nat. Rev. Cancer 10, 683–695.

Morris, J.P., 4th, Yashinskie, J.J., Koche, R., Chandwani, R., Tian, S., Chen, C.C., Baslan, T., Marinkovic, Z.S., Sánchez-Rivera, F.J., Leach, S.D., et al. (2019). α-Ketoglutarate links p53 to cell fate during tumour suppression. Nature 573, 595–599.

Morton, J.P., Timpson, P., Karim, S.A., Ridgway, R.A., Athineos, D., Doyle, B., Jamieson, N.B., Oien, K.A., Lowy, A.M., Brunton, V.G., et al. (2010). Mutant p53 drives metastasis and overcomes growth arrest/senescence in pancreatic cancer. Proc. Natl. Acad. Sci. USA 107, 246–251.

Mose, L.E., Wilkerson, M.D., Hayes, D.N., Perou, C.M., and Parker, J.S. (2014). ABRA: improved coding indel detection via assembly-based realignment. Bioinformatics 30, 2813–2815.

Mosteiro, L., Pantoja, C., Alcazar, N., Marión, R.M., Chondronasiou, D., Rovira, M., Fernandez-Marcos, P.J., Muñoz-Martin, M., Blanco-Aparicio, C., Pastor, J., et al. (2016). Tissue damage and senescence provide critical signals for cellular reprogramming in vivo. Science 354, aaf4445.

Muller, W.A. (2009). Mechanisms of transendothelial migration of leukocytes. Circ. Res. 105, 223–230.

Nandi, A., Estess, P., and Siegelman, M. (2004). Bimolecular complex between rolling and firm adhesion receptors required for cell arrest; CD44 association with VLA-4 in T cell extravasation. Immunity 20, 455–465.

Narita, M., Nūnez, S., Heard, E., Narita, M., Lin, A.W., Hearn, S.A., Spector, D.L., Hannon, G.J., and Lowe, S.W. (2003). Rb-mediated heterochromatin formation and silencing of E2F target genes during cellular senescence. Cell 113, 703–716.

Neves, J., Demaria, M., Campisi, J., and Jasper, H. (2015). Of flies, mice, and men: evolutionarily conserved tissue damage responses and aging. Dev. Cell 32, 9–18.

Öhlund, D., Handly-Santana, A., Biffi, G., Elyada, E., Almeida, A.S., Ponz-Sarvise, M., Corbo, V., Oni, T.E., Hearn, S.A., Lee, E.J., et al. (2017). Distinct populations of inflammatory fibroblasts and myofibroblasts in pancreatic cancer. J. Exp. Med. 214, 579–596.

Okumura, S., and Jänne, P.A. (2014). Molecular pathways: the basis for rational combination using MEK inhibitors in KRAS-mutant cancers. Clin. Cancer Res. 20, 4193–4199.

Olive, K.P., Jacobetz, M.A., Davidson, C.J., Gopinathan, A., McIntyre, D., Honess, D., Madhu, B., Goldgraben, M.A., Caldwell, M.E., Allard, D., et al. (2009). Inhibition of Hedgehog signaling enhances delivery of chemotherapy in a mouse model of pancreatic cancer. Science 324, 1457–1461.

Oubaha, M., Miloudi, K., Dejda, A., Guber, V., Mawambo, G., Germain, M.A., Bourdel, G., Popovic, N., Rezende, F.A., Kaufman, R.J., et al. (2016). Senescence-associated secretory phenotype contributes to pathological angiogenesis in retinopathy. Sci. Transl. Med. 8, 362ra144.

Panni, R.Z., Herndon, J.M., Zuo, C., Hegde, S., Hogg, G.D., Knolhoff, B.L., Breden, M.A., Li, X., Krisnawan, V.E., Khan, S.Q., et al. (2019). Agonism of CD11b reprograms innate immunity to sensitize pancreatic cancer to immunotherapies. Sci. Transl. Med. 11, eaau9240.

Plunkett, W., Huang, P., Xu, Y.Z., Heinemann, V., Grunewald, R., and Gandhi, V. (1995). Gemcitabine: metabolism, mechanisms of action, and self-potentiation. Semin. Oncol. 22 (4, Suppl 11), 3–10.

Poirier, J.T., Gardner, E.E., Connis, N., Moreira, A.L., de Stanchina, E., Hann, C.L., and Rudin, C.M. (2015). DNA methylation in small cell lung cancer defines distinct disease subtypes and correlates with high expression of EZH2. Oncogene *34*, 5869–5878.

Provenzano, P.P., Cuevas, C., Chang, A.E., Goel, V.K., Von Hoff, D.D., and Hingorani, S.R. (2012). Enzymatic targeting of the stroma ablates physical barriers to treatment of pancreatic ductal adenocarcinoma. Cancer Cell *21*, 418–429.

Rhim, A.D., Oberstein, P.E., Thomas, D.H., Mirek, E.T., Palermo, C.F., Sastra, S.A., Dekleva, E.N., Saunders, T., Becerra, C.P., Tattersall, I.W., et al. (2014). Stromal elements act to restrain, rather than support, pancreatic ductal adenocarcinoma. Cancer Cell *25*, 735–747.

Ribas, A., and Wolchok, J.D. (2018). Cancer immunotherapy using checkpoint blockade. Science *359*, 1350–1355.

Ribas, A., Lawrence, D., Atkinson, V., Agarwal, S., Miller, W.H., Jr., Carlino, M.S., Fisher, R., Long, G.V., Hodi, F.S., Tsoi, J., et al. (2019). Combined BRAF and MEK inhibition with PD-1 blockade immunotherapy in BRAF-mutant melanoma. Nat. Med. *25*, 936–940.

Rosow, D.E., Liss, A.S., Strobel, O., Fritz, S., Bausch, D., Valsangkar, N.P., Alsina, J., Kulemann, B., Park, J.K., Yamaguchi, J., et al. (2012). Sonic Hedgehog in pancreatic cancer: from bench to bedside, then back to the bench. Surgery *152* (3, Suppl 1), S19–S32.

Royal, R.E., Levy, C., Turner, K., Mathur, A., Hughes, M., Kammula, U.S., Sherry, R.M., Topalian, S.L., Yang, J.C., Lowy, I., and Rosenberg, S.A. (2010). Phase 2 trial of single agent Ipilimumab (anti-CTLA-4) for locally advanced or metastatic pancreatic adenocarcinoma. J. Immunother. *33*, 828–833.

Ruscetti, M., Leibold, J., Bott, M.J., Fennell, M., Kulick, A., Salgado, N.R., Chen, C.C., Ho, Y.J., Sanchez-Rivera, F.J., Feucht, J., et al. (2018). NK cell-mediated cytotoxicity contributes to tumor control by a cytostatic drug combination. Science *362*, 1416–1422.

Salmon, H., Remark, R., Gnjatic, S., and Merad, M. (2019). Host tissue determinants of tumour immunity. Nat. Rev. Cancer *19*, 215–227.

Samstein, R.M., Lee, C.H., Shoushtari, A.N., Hellmann, M.D., Shen, R., Janjigian, Y.Y., Barron, D.A., Zehir, A., Jordan, E.J., Omuro, A., et al. (2019). Tumor mutational load predicts survival after immunotherapy across multiple cancer types. Nat. Genet. *51*, 202–206.

Schaer, D.A., Beckmann, R.P., Dempsey, J.A., Huber, L., Forest, A., Amaladas, N., Li, Y., Wang, Y.C., Rasmussen, E.R., Chin, D., et al. (2018). The CDK4/6 Inhibitor Abemaciclib Induces a T Cell Inflamed Tumor Microenvironment and Enhances the Efficacy of PD-L1 Checkpoint Blockade. Cell Rep. *22*, 2978–2994.

Schafer, M.J., White, T.A., Iijima, K., Haak, A.J., Ligresti, G., Atkinson, E.J., Oberg, A.L., Birch, J., Salmonowicz, H., Zhu, Y., et al. (2017). Cellular senescence mediates fibrotic pulmonary disease. Nat. Commun. *8*, 14532.

Schumacher, T.N., and Schreiber, R.D. (2015). Neoantigens in cancer immunotherapy. Science *348*, 69–74.

Serrano, M., Lin, A.W., McCurrach, M.E., Beach, D., and Lowe, S.W. (1997). Oncogenic ras provokes premature cell senescence associated with accumulation of p53 and p16INK4a. Cell *88*, 593–602.

Sharpe, A.H., and Pauken, K.E. (2018). The diverse functions of the PD1 inhibitory pathway. Nat. Rev. Immunol. *18*, 153–167.

Shrimali, R.K., Yu, Z., Theoret, M.R., Chinnasamy, D., Restifo, N.P., and Rosenberg, S.A. (2010). Antiangiogenic agents can increase lymphocyte infiltration into tumor and enhance the effectiveness of adoptive immunotherapy of cancer. Cancer Res. *70*, 6171–6180.

Sieben, C.J., Sturmlechner, I., van de Sluis, B., and van Deursen, J.M. (2018). Two-Step Senescence-Focused Cancer Therapies. Trends Cell Biol. *28*, 723–737.

Siegel, R.L., Miller, K.D., and Jemal, A. (2019). Cancer statistics, 2019. CA Cancer J. Clin. *69*, 7–34.

Steele, C.W., Karim, S.A., Leach, J.D.G., Bailey, P., Upstill-Goddard, R., Rishi, L., Foth, M., Bryson, S., McDaid, K., Wilson, Z., et al. (2016). CXCR2 Inhibition Profoundly Suppresses Metastases and Augments Immunotherapy in Pancreatic Ductal Adenocarcinoma. Cancer Cell *29*, 832–845.

Sun, C., Hobor, S., Bertotti, A., Zecchin, D., Huang, S., Galimi, F., Cottino, F., Prahallad, A., Grernrum, W., Tzani, A., et al. (2014). Intrinsic resistance to MEK inhibition in KRAS mutant lung and colon cancer through transcriptional induction of ERBB3. Cell Rep. *7*, 86–93.

Sun, C., Mezzadra, R., and Schumacher, T.N. (2018). Regulation and Function of the PD-L1 Checkpoint. Immunity *48*, 434–452.

Tasdemir, N., Banito, A., Roe, J.S., Alonso-Curbelo, D., Camiolo, M., Tscharganeh, D.F., Huang, C.H., Aksoy, O., Bolden, J.E., Chen, C.C., et al. (2016). BRD4 Connects Enhancer Remodeling to Senescence Immune Surveillance. Cancer Discov. *6*, 612–629.

Vonderheide, R.H., and Bayne, L.J. (2013). Inflammatory networks and immune surveillance of pancreatic carcinoma. Curr. Opin. Immunol. *25*, 200–205.

Woo, R.A., and Poon, R.Y. (2004). Activated oncogenes promote and cooperate with chromosomal instability for neoplastic transformation. Genes Dev. *18*, 1317–1330.

Wu, N.Z., Klitzman, B., Dodge, R., and Dewhirst, M.W. (1992). Diminished leukocyte-endothelium interaction in tumor microvessels. Cancer Res. *52*, 4265–4268.

Xue, W., Zender, L., Miething, C., Dickins, R.A., Hernando, E., Krizhanovsky, V., Cordon-Cardo, C., and Lowe, S.W. (2007). Senescence and tumour clearance is triggered by p53 restoration in murine liver carcinomas. Nature *445*, 656–660.

Zirlik, K., and Duyster, J. (2018). Anti-Angiogenics: Current Situation and Future Perspectives. Oncol. Res. Treat. *41*, 166–171.

STAR★METHODS

KEY RESOURCES TABLE

REAGENT or RESOURCE	SOURCE	IDENTIFIER
Antibodies		
See Table S1 for Antibody information	N/A	N/A
Biological Samples		
Pancreatic cancer PDX: MSK-PR07	MSKCC/ This paper	N/A
Pancreatic cancer PDX: MSK-PR05	MSKCC/ This paper	N/A
Chemicals, Peptides, and Recombinant Proteins		
Trametinib (*in vitro*)	Selleck chemicals	Cat#S2673
Palbociclib (*in vitro*)	Selleck chemicals	Cat#S1116
Trametinib (*in vivo*)	LC Laboratories	Cat#T-8123
Palbociclib (*in vivo*)	LC Laboratories	Cat#P-7744
Gemcitabine	MSKCC Pharmacy	Cas#:122111-03-9
^{14}C-Gemcitabine	Moravek Biochemicals	Cat#MC 2246
Recombinant mouse IL-2	Biolegend	Cat#575402
Recombinant human IL-7	Peprotech	Cat#200-07
Recombinant human IL-15	Peprotech	Cat#200-15
Matrigel	Corning	Cat#354230
Solvable	Perkin Elmer	Cat#6NE9100
Ultima Gold	Perkin Elmer	Cat#6013321
Collagenase type V	Sigma	Cat#C9263
Culturex reduced growth factor basement membrane extract	R&D systems	Cat#3533-005-02
B27 supplement	Invitrogen	Cat#12634-028
hEGF	Peprotech	Cat#PMG8034
mNoggin	Peprotech	Cat#250-38
hFGF10	Peprotech	Cat#100-26
hLeu-Gastrin I	Sigma	Cat#G9145
N-acetylcysteine	Sigma	Cat#A9165
Nicotinamide	Sigma	Cat#N0636
Dynabeads Mouse T-Activator CD3/CD28	Thermo Fisher Scientific	Cat#11452D
PMA	Sigma	Cat#P8139
Ionomycin	Stem cell technologies	Cat#73724
GolgiStop	BD bioscience	Cat#554724
Trizol	Invitrogen	Cat#15596026
Biotinylated tomato lectin	Vector Laboratories	Cat#B1175
FITC-dextran (MW 2,000,000)	Sigma-Aldrich	Cat#52471
Pimonidazole	Hypoxyprobe	Cat#HP1-1000Kit
Critical Commercial Assays		
Human Cytokine/Chemokine Array 42-Plex Discovery Assay	Eve Technologies	Cat#HD42
Mouse Cytokine/Chemokine Array 31-Plex	Eve Technologies	Cat#MD31
CellTiter-Glo Viability Assay	Promega	Cat#G924A
eBioscience Foxp3 / Transcription Factor Staining Buffer Set	eBioscience	Cat#00-5523-00
TaqMan reverse transcription reagent	Thermo Fisher	Cat#N8080234
SYBR Green PCR master Mix	Thermo Fisher	Cat#4309155

(*Continued on next page*)

Continued

REAGENT or RESOURCE	SOURCE	IDENTIFIER
Deposited Data		
RNA sequencing data	This paper	GEO: GSE141684
RNA sequencing data	Ruscetti et al., 2018	GEO: GSE110397
Mouse whole exome sequencing	This paper	NCBI BioProject: PRJNA607826
Experimental Models: Cell Lines		
PANC-1 (human)	ATCC	Cat#CRL-1469; RRID: CVCL_0480
PU-8988T (human)	DSMZ	Cat#ACC-162; RRID:CVCL_1847
MiaPaca-2 (human)	ATCC	Cat#CRL-1420; RRID:CVCL_0428
3B11 (murine)	ATCC	Cat#CRL-2160; RRID:CVCL_5487
Pdx1-Cre; LSL-Kras$^{G12D/+}$*; LSL-p53*$^{R172H/wt}$ (*KPC*^{mut}) PDAC cells/organoids (murine)	This paper	N/A
Primary pancreatic fibroblasts from C57BL/6 mice	Cell Biologics, Inc.	Cat#C57-6201
Primary BMDM (Bone marrow-derived macrophages) from C57BL/6 mice	This paper	N/A
Experimental Models: Organisms/Strains		
Mouse: C57BL/6	Jackson laboratory	Cat#JAX:000664; RRID:IMSR_JAX:000664
Mouse: NOD-scid IL2Rγ^{null}: NOD.Cg-Prkdcscid Il2rgtm1Wjl/SzJ	Jackson laboratory	Cat#JAX:005557; RRID:IMSR_JAX:005557
Mouse: C57BL/6-Tg(TcraTcrb)1100Mjb/J	Jackson laboratory	Cat#JAX:003831; RRID:IMSR_JAX:003831
Mouse: LSL-K-ras G12D: B6.129S4-Krastm4Tyj/J	Jackson laboratory	Cat#JAX:008179; RRID:IMSR_JAX:008179
Mouse: Pdx1-Cre: B6.FVB-Tg(Pdx1-cre)6Tuv/J	Jackson laboratory	Cat#JAX:014647: RRID:IMSR_JAX:014647
Mouse: LSL-p53^{R172H}: p53LSL.R172H 129svj	Jackson laboratory	Cat#JAX:008652; RRID:IMSR_JAX:008652
Mouse: p53flox: B6.129P2-Trp53tm1Brn/J	Jackson laboratory	Cat#JAX:008462; RRID:IMSR_JAX:008462
Oligonucleotides		
shRNA sequence: Renilla: TAGATAAGCATTATAATTCCT	Chicas et al., 2010	N/A
shRNA sequence: p65: TATAGCTTCAGGGTACTCCATC	Chien et al., 2011	N/A
qPCR primer: p65 left: CTCAACTTCTGTCCCCAAGC	This paper	N/A
qPCR primer: p65 right: GAGGTACCATGGCTGAGGAA	This paper	N/A
qPCR primer: 36B4 left: GCTCCAAGCAGATGCAGCA	Morris et al., 2019	N/A
qPCR primer: 36B4 right: CCGGATGTGAGGCAGCAG	Morris et al., 2019	N/A
See Table S2 for additional qPCR primers	N/A	N/A
Recombinant DNA		
Plasmid: MSCV-Luciferase-IRES-GFP	This paper	N/A
Plasmid: LMP-shRNA	Chicas et al., 2010	N/A
Software and Algorithms		
Vevo LAB software	VisualSonic	VevoLab
Living Image software	Caliper Life Science	Cat#128113; RRID:SCR_014247
STAR	Dobin et al., 2013	RRID:SCR_015899;
featureCounts	Liao et al., 2014	RRID:SCR_012919; http://bioinf.wehi.edu.au/featureCounts/

(Continued on next page)

Continued

REAGENT or RESOURCE	SOURCE	IDENTIFIER
R	N/A	https://www.r-project.org
cutadapt	Martin, 2011	RRID:SCR_011841; http://gensoft.pasteur.fr/docs/cutadapt/1.6/guide.html
BWA	Li and Durbin, 2009	RRID:SCR_010910; http://bio-bwa.sourceforge.net
PICARD	N/A	RRID:SCR_006525; http://broadinstitute.github.io/picard/index.html
GATK	McKenna et al., 2010	RRID:SCR_001876; https://gatk.broadinstitute.org/
ABRA	Mose et al., 2014	RRID:SCR_003277; https://github.com/mozack/abra
muTect	Cibulskis et al., 2013	RRID:SCR_000559; https://software.broadinstitute.org/cancer/cga/mutect
DESeq2	Love et al., 2014	RRID:SCR_015687; https://bioconductor.org/packages/release/bioc/html/DESeq2.html
Trimmomatic	Bolger et al., 2014	RRID:SCR_011848; http://www.usadellab.org/cms/?page=trimmomatic
HTSeq	Anders et al., 2015	RRID:SCR_005514; https://htseq.readthedocs.io/en/release_0.11.1/
Enrichr	Kuleshov et al., 2016	RRID:SCR_001575; http://amp.pharm.mssm.edu/Enrichr
Other		
Vevo 2100 System ultrasound	VisualSonic	RRID:SCR_015816
Xenogen IVIS Spectrum imager	PerkinElmer	Cat#124262
Typhoon FLA 7000 laser scanner	GE healthcare	Cat#28-9558-09
Gentle MACS Octo dissociator with heaters	Miltenyi Biotech	Cat#130-096-427
Guava Easycyte	Millipore	Cat#0500-4008
ViiA 7 Real-Time PCR System	Invitrogen	Cat#4453536

LEAD CONTACT AND MATERIALS AVAILABILITY

Further information and requests for resources and reagents should be directed to and will be fulfilled by the Lead Contact, Scott W. Lowe (lowes@mskcc.org).

All unique/stable reagents generated in this study are available from the Lead Contact with a completed Materials Transfer Agreement.

EXPERIMENTAL MODEL AND SUBJECT DETAILS

Cell and organoid culture and derivation

PANC-1 (human, male), PU-8988T (human, female), MiaPaca-2 (human, male), and 3B11 (murine, male) cells were purchased from the American Type Culture Collection (ATCC) or DSMZ. Murine KPC^{mut} PDAC cell lines and organoids (male) were generated from PDAC arising in aged $Pdx1$-$Cre;Kras^{LSL-G12D/+};Trp53^{R172H/wt}$ (KPC^{mut}) mice. Cells were grown in "complete DMEM" containing 10% FBS and 100 IU/ml penicillin/streptomycin (P/S). Cells and organoids were maintained in a humidified incubator at 37°C with 5% CO_2. Only cell lines were used for *in vitro* studies. All cells and organoids used were negative for mycoplasma. All human cell lines were authenticated by their source repository.

To generate KPC^{mut} PDAC cell lines, tumors arising in *Pdx1-Cre; LSL-Kras$^{G12D/+}$; LSL-p53$^{R172H/wt}$* (KPC^{mut}) mice were minced with scissors and the dissociated in 1 mg/ml Collagenase type V (C9263; Sigma) and 2U/ml Dispase II (04942078001; Roche) diluted in Hanks Buffered Saline Solution (HBSS) (14025-076; Life technologies) at 37°C with mild agitation for up to 1 hour. The cell suspension was then plated on 10 cm^2 culture dishes coated with 100 μg/ml collagen (PureCol) (5005; Advanced Biomatrix) and grown in complete DMEM. Primary cultures were passaged at least 3 times to remove fibroblast contamination. KPC^{mut} PDAC cells were then transduced with a Luciferase (Luc)-GFP co-expression vector to visualize them *in vivo*. Luc-GFP constructs were cloned into MSCV-based vectors and retroviruses were packaged by co-transfection of Gag-Pol expressing 293 T cells with expression constructs and envelope vectors (VSV-G) using the calcium phosphate method. Following transduction, cells were purified by FACS sorting the GFP$^+$ population on a FACSAria (BD Biosciences).

KPC^{mut} PDAC organoids were generated by mincing and dissociating tumors arising in *Pdx1-Cre; LSL-Kras$^{G12D/+}$; LSL-p53$^{R172H/wt}$* (KPC^{mut}) mice with collagenase and dispase as described above. Unfiltered, dissociated tissue was then seeded in growth factor-reduced (GFR) Matrigel (BD) and cultured in advanced DMEM/F12 supplemented with the following: 1% P/S, 2mM glutamine, 1X B27 supplement (12634-028; Invitrogen), 50ng/ml hEGF (PMG8043; Peprotech), 100ng/ml mNoggin (250-38; Peprotech), 100ng/ml hFGF10 (100-26; Peprotech), 10 nM hLeu-Gastrin I (G9145, Sigma), 1.25mM N-acetylcysteine (A9165; Sigma), 10mM Nicotinamide (N0636; Sigma), and R-spondin1 conditioned media (10% final). Organoids were passaged every 3-4 days.

Primary murine pancreatic fibroblasts from C57BL/6 mice were purchased from Cell Biologics, Inc. and grown in complete fibroblast media (M2267). To generate primary bone marrow-derived macrophages (BMDMs), bone marrow was flushed from the hind limbs of 9 week old female C57BL/6 mice under sterile conditions, passed through a 40 μm strainer and cultured in 30 mL Teflon Bags (PL-30; PermaLife) in DMEM supplemented with 10% FBS and 10 ng/ml of recombinant mouse CSF1 (R&D systems). Bone marrow cells were cultured for 7 days, refreshing CSF1-containing media every other day, after which they were referred to as BMDMs.

Animal Studies

All mouse experiments were approved by the Memorial Sloan Kettering Cancer Center (MSKCC) Internal Animal Care and Use Committee under MSKCC IACUC protocol 11-06-018. Mice were maintained under specific pathogen-free conditions, and food and water were provided *ad libitum*.

KPC^{flox} PDAC GEMM

Trp53$^{fl/fl}$, LSL-Kras$^{G12D/+}$, and *Pdx1-Cre* strains on a C57BL/6 background were interbred to obtain *Pdx1-Cre; LSL-Kras$^{G12D/+}$; Trp53$^{fl/wt}$* (KPC^{flox}) mice. Both male and female KPC^{flox} mice ranging from 2.5 to 12 months of age were used for treatment studies upon confirmation of tumor development. Mice were monitored for tumor development by ultrasound, and enrolled and randomized into treatment groups once tumors reached 100-300 mm^3. Ultrasound imaging was repeated every 2 weeks during treatment to assess changes in pancreas tumor burden. For immunohistochemical and flow cytometry analysis, mice were treated for 2 weeks with indicated drugs. Upon sacrifice pancreas tumor tissue was allocated for 10% formalin fixation, OCT frozen blocks, and snap frozen tissue, and the rest used to generate single cell suspensions for flow cytometry analysis.

KPC^{mut} PDAC organoid transplant model

For orthotopic engraftment of KPC^{mut} PDAC organoids derived from *Pdx1-Cre; LSL-KRAS$^{G12D/+}$; Trp53$^{R172H/wt}$* (KPC^{mut}) tumors, 8-10 week old C57BL/6 or NOD-*scid* IL2Rγ^{null} (NSG) female mice (Jackson Laboratory) were first anesthetized using isoflurane and an incision was made in the left abdominal side. Organoids (approximately 1-3x10^5 cells/mouse) were prepared from cultures. Organoid cultures were dissociated with TrypLE (ThermoFisher; 12604-021) and finally resuspended in 25 μL of growth factor reduced Matrigel (354230; Corning) diluted 1:1 with cold adDMEM F/12 media supplemented with 2mM glutamine. The organoid suspension was injected into the tail region of the pancreas using a Hamilton Syringe. Successful injection was verified by the appearance of a fluid bubble without signs of intraperitoneal leakage. The abdominal wall was sutured with absorbable Vicryl sutures (Ethicon), and the skin was closed with wound clips (CellPoint Scientific Inc.). Mice were monitored for tumor development by ultrasound (anywhere from 1.5-6 months post-transplantation), and enrolled and randomized into treatment groups once tumors reached 100-300 mm^3. Ultrasound imaging was repeated every 2 weeks during treatment to assess changes in pancreas tumor burden. For immunohistochemical and flow cytometry analysis, mice were treated for 2 weeks with indicated drugs. Upon sacrifice pancreas tumor tissue was allocated for 10% formalin fixation, OCT frozen blocks, and snap frozen tissue, and the rest used to generate single cell suspensions for flow cytometry analysis.

KPC^{mut} PDAC cell line transplant model

To rapidly generate orthotopic PDAC tumors in immunocompetent mice for immunophenotyping experiments, 5x10^4 KPC^{mut} PDAC cells expressing luciferase and GFP (LUC-GFP) were orthotopically transplanted into the pancreas of 8-10 week old C57BL/6 female mice as described above. Mice were monitored for tumor development (5-8 days post-transplantation) by bioluminescence imaging (BLI) on a Xenogen IVIS Spectrum imager (PerkinElmer) before being randomized into various study cohorts. For immunohistochemical and flow cytometry analysis, mice were treated for 2 weeks with indicated drugs. Upon sacrifice pancreas tumor tissue was allocated for 10% formalin fixation, OCT frozen blocks, snap frozen tissue, and the rest for flow cytometric analysis.

Patient-Derived Xenograft (PDX) models

5-7 week old female NOD-*scid* IL2Rγ^{null} (NSG) mice were used for animal experiments with patient-derived xenografts (PDXs). PDAC PDXs used for preclinical studies were selected based upon presence of a robust stromal compartment and resistance to gemcita-

bine chemotherapy. MSK-PR07 is a PDAC PDX harboring mutations in *KRAS* (*G12D*) and *p53* (*L344Q*) and derived from a patient treated with three rounds of chemotherapy: 1) gemcitabine and cisplatin, 2) FOLFIRINOX, and 3) gemcitabine and abraxane. MSK-PR05 is a PDAC PDX derived from a patient previously treated with gemcitabine, abraxane, and the HA degrading agent PEGPH20. Tumors were cut into pieces and inserted into a pocket in the subcutaneous space as previously described (Poirier et al., 2015). Following inoculation, mice were monitored daily, weighed twice weekly, and caliper measurements begun when tumors became visible. Tumor volume was calculated using the following formula: tumor volume = $(D \times d^2)/2$, in which D and d refer to the long and short tumor diameter, respectively. When tumors reached a size of 100-200 mm^3, mice were randomized based on starting tumor volume (caliper measurements) and enrolled into treatment groups. Tumor size and mouse weights were recorded twice weekly. Experimental endpoints were achieved when tumors reached 2000 mm^3 or became ulcerated.

METHOD DETAILS

Compounds

Trametinib (S2673) and palbociclib (S1116) were purchased from Selleck chemicals for *in vitro* studies. Drugs for *in vitro* studies were dissolved in DMSO (vehicle) to yield 10 mM stock solutions and stored at -80°C. For *in vitro* studies, growth media with or without drugs was changed every 2-3 days. For *in vivo* studies, trametinib (T-8123) and palbociclib (P-7744) were purchased from LC Laboratories. Trametinib was dissolved in a 5% hydroxypropyl methylcellulose and 2% Tween-80 solution (Sigma), and palbociclib in sodium lactate buffer (pH 4). Gemcitabine was purchased from the MSKCC pharmacy and diluted accordingly in saline.

Short-hairpin RNA (shRNA) knockdown

MiR30-based shRNAs targeting *p65* and *Renilla* (as a control) were cloned into the XhoI EcoRI locus of the MSCV-based LMP vector (Chicas et al., 2010; Chien et al., 2011). Retroviruses were packaged by co-transfection of Gag-Pol expressing 293 T cells with expression constructs and envelope vectors (VSV-G) using the calcium phosphate method, and virus containing media applied to target *KPC^{mut}* cells. Infected cells were selected with 1 μg/ml puromycin for 5 days. Knockdown was confirmed by qRT-PCR and immunohistochemistry (following transplantation into C57BL/6 mice).

For p65 knockdown studies in *KPC^{mut}* organoids, virus containing media was collected in AdDMEM supplemented with 1X P/S and 2mM glutamine and mixed 1:1 with full organoid media. Organoids were treated with virus overnight twice and subsequently selected for 1 week with 1μg/ml puromycin. Knockdown was confirmed by immuhistochemistry following transplantation into C57BL/6 mice.

Preclinical drug studies

Mice were treated with vehicle, trametinib (1 mg/kg or 0.3 mg/kg body weight), and/or palbociclib (100 mg/kg body weight) *per os* for 4 consecutive days followed by 3 days off treatment. Gemcitabine (100 mg/kg body weight) was administered twice per week, or an α-PD-1 antibody (200 μg; RMP1-14, BioXcell) was given 3 times per week by intraperitoneal (IP) injection alone or in combination with trametinib and palbociclib treatment concurrently. Gemcitabine was also given on an alternating treatment schedule with T/P, where T/P was given on 4 consecutive days followed by 3 days off treatment for 1 week, followed by gemcitabine administration twice a week for 1 week. For PDX models propogated in NSG mice, gemcitabine was administered once per week. No obvious toxicities were observed in the vehicle- or drug-treated animals as assessed by changes in body weight (taking tumor size into account).

Neutralizing antibody studies

High doses of an α-VEGFR-2 blocking antibody (800 μg; DC101, BioXcell) were administered twice per week by IP injection to block neo-vascularization. For NK cell depletion, mice were injected IP with an α-NK1.1 antibody (250 μg; PK136, BioXcell) twice per week. For T cell depletion, mice were injected IP with either an α-CD4 (200 μg; GK1.5, BioXcell) or α-CD8 antibody (200 μg; 2.43, BioXcell) twice per week. Depletion of NK, CD4$^+$, and CD8$^+$ T cells was confirmed by flow cytometric and immunohistochemical analysis of pancreas tumor tissue. For neutralization of cell surface molecules that mediate immune-endothelial interactions, mice were injected IP with either an α-VCAM-1 (200 μg; M/K-2.7, BioXcell), α-PSGL-1 (50 μg; 4RA10, BioXcell), or α-ICAM-1 antibody (200 μg; YN1/1.7.4, BioXcell) twice per week. For neutralization of SASP factors, mice were injected IP with either an α-VEGFR2 (800 μg; DC101, BioXcell), α-IL-6 (200 μg; MP5-20F3, BioXcell), α-TGF-β (300 μg; 1D11.16.8, BioXcell), α-IL-1β (200 μg; B122, BioXcell), CCL-5 (50 μg; 53405, R&D systems), or CXCL-1 antibody (25 μg, 48415, R&D systems) twice per week.

Ultrasound Imaging

High-contrast ultrasound imaging was performed on a Vevo 2100 System with a MS250 13- to 24-MHz scanhead (VisualSonics) to stage and quantify pancreas tumor burden. Tumor volume was analyzed using Vevo LAB software.

Bioluminescence imaging

Bioluminescence imaging (BLI) was used to track luciferase expression in orthotopically transplanted *KPC^{mut}* PDAC tumor cells expressing a LUC-GFP reporter. Mice were injected IP with luciferin (5 mg/mouse; Gold Technologies) and then imaged on a Xenogen IVIS Spectrum imager (PerkinElmer) 10-15 minutes later for 60 s. Quantification of luciferase signaling was analyzed using Living Image software (Caliper Life Sciences).

Tumor perfusion, permeability, and drug uptake assays

PDAC-bearing *KPC^mut* organoid transplant and *KPC^flox* GEMM mice were pretreated for 2 weeks with vehicle or combined trametinib (1 mg/kg body weight) and palbociclib (100 mg/kg body weight) *per os* for 4 consecutive days followed by 3 days off treatment. To assess vascular permeability following treatment, 1 mg of FITC–dextran (MW 2,000,000; Sigma-Aldrich) was administered intravenously in the lateral tail vein 30 minutes before sacrifice. Similarly, to measure vascular perfusion/patency, 100 μg of biotinylated tomato lectin (B1175; Vector Laboratories) was injected intravenously 1 hour before sacrifice. To assess hypoxia in PDAC tissue, 60 mg/kg hydoxyprobe (Hypoxyprobe; HP1-100 kit) was administered by IP injection 30 minutes prior to euthanasia.

To assess gemcitabine uptake into pancreas tumors, ^{14}C-gemcitabine (specific activity 58.8 mCi/mmol; Moravek Biochemicals) was administered in sterile saline by IP injection at 2 μCi/animal. Animals were euthanized 2 hours after ^{14}C-gemcitabine administration, and tumor tissue, as well as tissue from normal pancreas and other organs were collected for downstream analysis. Tumors were divided for scintillation counting and autoradiography. Fragments of tumor (approximately 100 mg) were weighed and dissolved in Solvable™ (Perkin Elmer, Waltham MA), followed by 100 mL hydrogen peroxide, and counted in 7 mL Ultima Gold™ (Perkin Elmer). Activity was expressed as disintegrations per minute (dpm)/milligram. Autoradiographs were obtained from flash-frozen tumor cryosections, exposed to GE storage phosphor screens for 7 days and read with the Typhoon FLA 7000 laser scanner (GE Healthcare Life Sciences, Pittsburgh, PA). Before exposure, slides were marked with nail polish containing a blue dye and ^{14}C to permit registration of autoradiographic and microscopic images.

Flow cytometry

For *in vivo* sample preparation, tumors were isolated following removal of the spleen and normal pancreas tissue, and allocated for 10% formalin fixation, OCT frozen blocks, snap frozen tissue, and flow cytometry analysis following 2-week treatment. To prepare single cell suspensions for flow cytometry analysis, tumors were minced with scissors into small pieces and placed in 5ml of collagenase buffer (1x HBSS w/ calcium and magnesium (GIBCO), 1 mg/ml Collagenase V (C9263; Sigma), and 0.1 mg/ml DNase I (DN25; Sigma)). Samples were then transferred to C tubes and processed using program 37C_m_TDK1_1 on a gentleMACS Octo dissociator with heaters (Miltenyi Biotec). Dissociated tissue was passaged through a 70 μm cell strainer and centrifuged at 1500 rpm x 5 minutes. Red blood cells were lysed with ACK lysis buffer (Quality Biological) for 5 minutes, and samples were centrifuged and resuspended in PBS supplemented with 2% FBS. Samples were blocked with anti-CD16/32 (FC block, BD Pharmigen) for 20 minutes and then incubated with the following antibodies for 30 minutes on ice: CD45 (30-F11), NK1.1 (PK136), CD3 (17A2), CD8 (53-6.7), CD4 (GK1.5), Gr-1 (RB6-8C5), PD-L1 (CD274;10F.9G2), CD31 (390), VCAM-1 (CD106;MVCAM.A), P-selectin (CD62P; RMP-1), CD69 (H1.2F3), CTLA-4 (CD152; UC10-4B9), 2B4 (CD244.2; m2B4 (B6)458.1), VLA-4 (CD49d; R1-2), F4/80 (BM8), PD-1 (CD279; RMP1-30), CD44 (IM7), CD86 (GL-1), CD206 (MMR), Ly6G (1A8) (Biolegend); CD11b (M1/70) (BD Biosciences); MHC-I (H-2k^b; AF6-88.5.5.3), LAG-3 (eBioC9B7W) (eBioscience); and ICAM-1 (AB796) (R&D Systems). DAPI was used to distinguish live/dead cells, and tumor cells were gated as GFP$^+$ in the *KPC^mut* PDAC cell line transplant model where tumor cells harbor a LUC-GFP construct. Flow cytometry was performed on an LSRFortessa, and data were analyzed using FlowJo (TreeStar).

In vivo degranulation assay

Mice were injected intravenously with 250 μL of a solution containing 25 μg anti-CD107a PE (ID4B, Biolegend) in 1X PBS 3 hours before mice were euthanized. Pancreas tumor tissue was then isolated, dissociated, stained with cell surface antibodies, and analyzed by flow cytometry as described above.

Immunohistochemistry and immunofluorescence

Tissues were fixed overnight in 10% formalin, embedded in paraffin, and cut into 5 μm sections. Haematoxylin and eosin (H&E) and Masson's trichrome staining were performed using standard protocols. For frozen sections, pancreata were directly embedded in OCT (VWR Chemicals, 361603E) and frozen on dry ice. For immunohistochemical and immunofluorescence analysis, sections were de-paraffinized, rehydrated, and boiled in a microwave for 15 minutes in 10 mM citrate buffer (pH 6.0) for antigen retrieval. Antibodies were incubated overnight at 4°C.

The following primary antibodies were used: pERK$^{T202/Y204}$ (4370), cleaved caspase-3 (CC3) (9664), PDGFRβ (3169), NF-κB (p65;8242) (Cell Signaling); Ki67 (AB16667), CD31 (AB28364), α-smooth muscle actin (αSMA;AB5694), CD3 (AB5690), granzyme B (AB4059), LYVE1 (AB14917) (Abcam); pRB$^{S807/S811}$ (Sc-16670) (Santa Cruz); NKp46 (AF2225), VCAM-1 (AF643), ICAM-1 (AF796) (R&D Systems); FOXP3 (14-5773-82), CD8 (14-0808-82) (eBioscience); mouse pan-endothelial cell antigen (MECA-32) (University of Iowa); P-selectin (LS-B3578) (LSBio); FAP (ABT11) (Millipore); CD31 (DIA-310) (Dianova); biotinylated hyaluronic acid binding protein (HABP) (AMS.HKD-BC41; AMSBIO); and cytokeratin 19 (CK19; TROMA-III) (DSHB).

HRP-conjugated secondary antibodies (Vectastain Elite ABC HRP Kits) were applied for 30 minutes and visualized with DAB (Vector Laboratories; SK-4100), or secondary Alexa Fluor 488 or 594 dye-conjugated antibodies (Life Technologies) applied for 1 hour at room temperature. Fluorescence antibody-labeled slides were mounted with Prolong Gold Antifade mountant (Prolong Molecular Probes; P36934) after counterstaining with DAPI.

Analysis of protein adducts of reductively activated pimonidazole were identified through immunohistochemistry in fixed tissues with a monoclonal antibody against hypoxyprobe-1 according to the manufacturer's protocol (Hypoxyprobe; HP1-100 kit). To assess lectin perfusion, PDAC tissue sections isolated from mice injected with biotinylated tomato lectin (B1175; Vector Laboratories) were

stained with a fluorescein-conjugated streptavidin (SA-5001: Vector Laboratories) for 30 minutes and processed as described above.

SA-β-gal staining

SA-β-gal staining was performed at pH 6.0 for human cells and 5.5 for mouse cells and tissue. Fresh frozen sections of pancreas tumor tissue, or adherent cells plated in 6-well plates and treated for 8 days in culture with vehicle (DMSO), trametinib (25nM), and/or palbociclib (500nM), were fixed with 0.5% Gluteraldehyde in PBS for 15 min, washed with PBS supplemented with 1mM $MgCl_2$, and stained for 5–8 hours in PBS containing 1 mM $MgCl_2$, 1mg/ml X-Gal, and 5 mM each of Potassium ferricyanide and Potassium ferrocyanide. Tissue sections were counterstained with eosin. 5 high power fields per well/section were counted and averaged.

Conditioned Media collection

PDAC cells were plated in 6-well plates and treated for 6 days in the presence or absence of trametinib (25nM) and/or palbociclib (500nM). On day 6, 2 mL of serum-free or complete DMEM was added to each well and cells were incubated an additional 48 hours in the presence or absence of drugs. Conditioned media was then collected and the cells were trypsinized and counted using a cellometer (Nexcelom Biosciences). After normalizing the concentration of the conditioned media by the cell count, conditioned media from vehicle- or T/P-pretreated KPC^{mut} PDAC tumor cells was then applied to endothelial cells, fibroblasts, and bone marrow-derived macrophages to assess changes in growth, or used for downstream cytokine array analysis.

Cytokine array

Conditioned media samples (collected in complete DMEM) from treated PDAC cell lines or primary pancreatic murine fibroblasts (plated in triplicate) were normalized based on cell number by diluting with complete DMEM. Aliquots (50 μl) of the conditioned media were analyzed using multiplex immunoassays designed for human (Human Cytokine/Chemokine Array 42-Plex Discovery Assay) or mouse (Mouse Cytokine/Chemokine Array 31-Plex or MMP Discovery Array 5-Plex Discovery Assay) from Eve Technologies. Biological replicates were averaged to determine cytokine levels. Heatmaps display relative cytokine expression values normalized to vehicle-treated samples.

In vitro cell growth assays

KPC^{mut} tumor cells were treated with vehicle or combined trametinib (25nM) and palbociclib (500nM) for 6 days, and conditioned serum-free DMEM was collected as described above. Filtered conditioned media (CM) or basal serum-free media was then applied to various primary and established cell lines. To measure endothelial cell and fibroblast growth, 5,000 3B11 murine endothelial cells and 10,000 primary murine pancreatic fibroblasts were plated in 24-well dishes. Cells were counted daily in quadruplicate using a Guava Easycyte (Millipore) and media changed every 3 days. To analyze the impact on macrophage growth, 10,000 bone marrow-derived macrophages (BMDMs) were plated in 96 well dishes and, one day thereafter, were exposed to CM or basal serum-free media diluted 1:2 in DMEM containing 10% FBS and 10 ng/mL Csf1. Cell viability was assessed using the CellTiter-Glo Viability Assay (Promega) according to the manufacturer's protocol.

In vitro endothelial tube formation assay

3B11 endothelial cells were plated in 48 well dishes coated with a 150 μL layer of Cultrex reduced growth factor basement membrane extract (3533-005-02; R&D Systems) and cultured in basal or serum-free conditioned DMEM media for 8 hours. Images of tube structures were captured on a INCell 6000 high-content imager (GE Healthcare Life Sciences) at 10x magnification.

T cell functionality assays

Spleens were harvested from female OT-1 mice (Jackson laboratory), mechanically disrupted by passing them through a 70 μm cell strainer, and centrifuged at 1500 rpm x 5 minutes. Red blood cells were lysed with ACK lysis buffer (Quality Biological) for 5 minutes. Total splenocytes or $CD8^+$ T cells FACS sorted on a Sony MA900 were then activated with CD3/CD28 Dynabeads (one bead/T cell, Thermo Fisher) and cultured in presence of IL-2 (2 ng/ml; Biolegend), IL-7 (2.5 ng/ml; Peprotech) and IL-15 (50 ng/ml; Peprotech) in complete RPMI media supplemented with 10% FBS and 100 IU/ml penicillin/streptomycin for four to six days prior to co-culture assays with PDAC cells.

To generate KPC^{mut} PDAC cells expressing chicken ovalbumin (KPC^{mut}-OVA), KPC^{mut} PDAC cells were transduced with a pCDH-derived lentiviral vector expressing amino acids 48-386 of the chicken ovalbumin protein under the control of a minimal CMV promoter and a blasticidin resistance cassette under the control of an EF1-α promoter. Lentiviruses were packaged by co-transfection of 293 T cells with the expression construct, envelope vector (VSV-G), and lenti Gag-Pol vector using the calcium phosphate method. Selection of OVA-expressing tumor cells was performed with blasticidin (10 μg/ml; Thermo Fisher) over 3 days.

For analysis of expression of cytokines and activation markers on $CD8^+$ T cells, total splenocytes were co-cultured for 4 hours with KPC^{mut} or KPC^{mut}-OVA PDAC tumor cells (pretreated with vehicle or combined trametinib (25nM) and palbociclib (500nM) (T/P) for 8 days) at a 1:1 effector to target (E:T) ratio in complete RPMI. To functionally block MHC-I activity, T cells were also co-cultured with tumor cells in the presence of a H-2k^b blocking antibody (40 μg/ml; Y-3, BioXcell). As a positive control for T cell activation, cells were treated for 4 hours with PMA (20 ng/ml, sigma aldrich) and Ionomycin (1 μg/ml, stem cell technologies). Co-culture experiments were

performed either in the absence (surface staining) or in the presence (intracellular cytokine staining) of GolgiStop (BD Biosciences). Cell surface staining was performed with CD8 (53-6.7), CD44 (IM7) and CD69 (H1.2F3) antibodies (Biolegend) for those cells that were not pretreated with GolgiStop. GolgiStop-pretreated cells were first stained with CD8 (53-6.7) antibody, then intracellular staining was performed using the Foxp3/transcription factor staining buffer set (eBioscience), where cells were fixed, permeabilized, and then stained with IFN-γ (XMG1.2; TONBO Biosciences) and TNF-α (MP6-XT22; eBiosciences) antibodies. Expression of cytokines and activation markers was evaluated by gating on CD8$^+$ T cells. Flow cytometry was performed on an LSRFortessa, and data were analyzed using FlowJo (TreeStar).

To assess the functionality of PDAC-infiltrating lymphocytes *ex vivo*, PDAC tumors isolated from *KPC^{mut}* organoid transplant mice treated for two weeks with vehicle, combined trametinib (1 mg/kg body weight) and palbociclib (100 mg/kg), and/or an α-PD-1 antibody (200 μg; RMP1-14, BioXcell) were dissociated into single cell suspensions, incubated for 4 hours with PMA (20 ng/ml, sigma aldrich) and Ionomycin (1 μg/ml, stem cell technologies), and stained with CD8, IFN-γ, and TNF-α antibodies for flow cytometry analysis as above.

qRT-PCR

For analysis of macrophage polarization following T/P treatment, total RNA was extracted from CD45$^+$CD11b$^+$Gr-1$^-$F4/80$^+$ macrophages (sorted on a FACSAria (BD Biosciences)) isolated from *KPC^{mut}* transplant PDAC tumors treated for 2 weeks with vehicle or combined trametinib (1 mg/kg body weight) and palbociclib (100 mg/kg) using TRIzol RNA Isolation Reagents (Invitrogen). Total RNA was also extracted from indicated *KPC^{mut}* PDAC cell lines following 8 day treatment with vehicle or trametinib (25nM) and palbociclib (500nM) in culture using the RNeasy Mini Kit (QIAGEN). Complementary DNA (cDNA) was obtained using the TaqMan reverse transcription reagents (Applied Biosystems). Real-time PCR was performed in duplicate or triplicate using SYBR Green PCR Master Mix (Applied Biosystems) on the ViiA 7 Real-Time PCR System (Invitrogen). 36B4 served as an endogenous normalization control.

High throughput RNA-sequencing (RNA-seq) analysis

For RNA-seq analysis of the transcriptional profiles of tumor cells from *KPC^{mut}* transplant PDAC tumors in mice treated for 2 weeks with vehicle or combined trametinib (1 mg/kg body weight) and palbociclib (100 mg/kg), total RNA was extracted from GFP$^+$ tumor cells (sorted on a FACSAria (BD Biosciences)) using the RNeasy Mini Kit (QIAGEN). Purified polyA mRNA was subsequently fragmented, and first and second strand cDNA synthesis performed using standard Illumina mRNA TruSeq library preparation protocols. Double stranded cDNA was subsequently processed for TruSeq dual-index Illumina library generation. For sequencing, pooled multiplexed libraries were run on a HiSeq 2500 machine on RAPID mode. Approximately 10 million 76bp single-end reads were retrieved per replicate condition. Resulting RNA-Seq data was analyzed by removing adaptor sequences using Trimmomatic (Bolger et al., 2014), aligning sequencing data to GRCh37.75(hg19) with STAR (Dobin et al., 2013), and genome wide transcript counting using HTSeq (Anders et al., 2015) to generate a RPKM matrix of transcript counts. Genes were identified as differentially expressed using R package DESeq2 with a cutoff of absolute log$_2$FoldChange $\geq$ 1 and adjusted p value < 0.05 between experimental conditions (Love et al., 2014). Functional enrichments of these differential expressed genes were performed with enrichment analysis tool Enrichr (Kuleshov et al., 2016) and the retrieved combined score (log(p value) * z-score) was displayed.

To assess expression of antigen presentation and processing genes in human PDAC cell lines treated with vehicle (DMSO), trametinib (25nM), and/or palbociclib (500nM) for 8 days in culture, we interrogated a previously published RNA-seq dataset from Ruscetti et al. (2018) (GEO: GSE110397). Heatmaps display the fold change in RPKM expression values normalized to vehicle-treated samples.

Clustering and Gene Set Enrichment Analysis (GSEA)

Principal component analysis was performed using the DESeq2 package in R. Gene expressions of RNA-Seq data were clustered using hierarchical clustering based on one minus pearson correlation test. For pathway enrichment analysis, the weighted GSEA Preranked mode was used on a set of curated signatures in the molecular signatures database (MSigDB v6.2) (https://www.broadinstitute.org/gsea/msigdb/index.jsp). From 17,810 signatures, signatures with 15-500 genes were only considered for the further analyses. From the results, enriched signatures with an adjusted *p* value less than 0.05 were considered as statistically significant.

Whole exome sequencing (WES)

WES was conducted on genomic DNA (gDNA) isolated from PDAC tumors harvested at survival endpoint from *KPC^{mut}* organoid transplant and *KPC^{flox}* GEMM mice. gDNA was also isolated from peripheral blood of a non-tumor bearing C57/BL6 mouse to generate a baseline reference sequence. gDNA was isolated using the DNeasy Blood & Tissue Kit (QIAGEN) and WES was conducted and sequenced by BGI. The data was then processed through the Illumina (HiSeq) Exome Variant Detection Pipeline for detecting variants by the Bioinformatics Core at MSKCC. First, the FASTQ files were processed to remove any adaptor sequences at the end of the reads using cutadapt (v1.6). The files were then mapped using the BWA mapper (bwa mem v0.7.12). After mapping the SAM files were sorted and read group tags added using the PICARD tools. After sorting in coordinate order the BAMs were processed with PICARD MarkDuplicates. The marked BAM files were then processed using the GATK toolkit (v 3.2) according to the best

practices for tumor normal pairs. They were first realigned using ABRA (v 0.92) and then the base quality values recalibrated with the BaseQRecalibrator. Somatic variants were then called in the processed BAMs using muTect (v1.1.7) for SNV and the Haplotype caller from GATK with a custom post-processing script to call somatic indels. Mutations that occurred more than once among all *in vivo* mouse PDAC tumor samples, but did not appear *in vitro* prior to transplantation, were removed. Based on the information provided by Agilent SureSelect XT Mouse All Exon Kit, the total exome coverage was about 49.6MB. This coverage length was used to calculate mutations per MB and compared with publicly available mutational data downloaded from (Alexandrov et al., 2013).

QUANTIFICATION AND STATISTICAL ANALYSIS

Histological and Image Analysis

To measure endothelial tube formation *in vitro*, four fields per well were analyzed and grouped by well using Cell Profiler. In order to outline the whole cell/tube profile, the image was first processed using the EnhanceEdges function, followed by Smooth filters. The subsequent image was then thresholded to produce an outline object for the tube formation within each field. This object mask was then transformed with the skeletonize mask function and measurements on this skeleton used to determine tube length.

Quantification of the number of CD31$^+$ blood vessels (mean vessel density), SA-β-gal$^+$ senescent cells, Ki67$^+$ proliferating cells, CC3$^+$ dead/dying cells, CD3$^+$ and CD8$^+$ T cells, and other immune and stromal cell types was performed on 5 high power 20x fields per section that were counted and averaged. The distance between blood vessels and tumor cells was determined for 20 randomly chosen blood vessels, and the distance to the four nearest tumors cells was measured and averaged using ImageJ software. Assessment of stromal reactivity was performed by scoring the number and intensity of the pixels by color deconvolution using Aperio software (IHC score) on trichrome, αSMA, and HA-stained sections.

Metastatic burden in the lungs and liver, as well as necrotic areas in primary PDAC lesions, were quantified from low magnification (1x) H&E-stained whole tissue sections. Tumor necrosis was assessed by the percentage of total tumor area covered in necrotic tissue on H&E-stained sections using ImageJ software.

To quantify colocalization of various markers with blood vessels, slides were first scanned with Pannoramic 250 Flash scanner (3DHistech, Hungary) using 20x/0.8NA objective lens. Regions of interest around the tissues were then drawn and exported as .tif files from these scans using Caseviewer (3DHistech, Hungary.) These images were then analyzed using ImageJ/FIJI (NIH, USA) where a median filter, thresholding, and watershedding were used to segment the nuclei in the DAPI channel. These segmented nuclei were then used to determine percent overlap between the different combinations of markers with their respective thresholds in order to quantify colocalization.

To assess lectin perfusion, PDAC tissue sections were co-stained with CD31, and the percentage of lectin$^+$ blood vessels was quantified. Hypoxia was assessed as the percentage of tumor tissue containing activated pimonidazole using ImageJ software. Vascular permeability was assessed by percentage of total tumor area that was FITC-dextran positive on fresh frozen sections.

Statistical analysis

Statistical significance between groups was calculated by two-tailed Student's t test unless specified otherwise in the figure legend. Data are expressed as mean $\pm$ SEM. Group size was determined on the basis of the results of preliminary experiments and no statistical method was used to predetermine sample size. The indicated sample size (n) represents biological replicates. Group allocation and outcome assessment were not performed in a blinded manner. All samples that met proper experimental conditions were included in the analysis. Survival was measured using the Kaplan–Meier method. Statistical significance was determined by one- and two-way ANOVA, Student's t test, and log-rank test using Prism 6 software (GraphPad Software) as indicated. Significance was set at $p < 0.05$.

DATA AND CODE AVAILABILITY

The accession number for the RNA-seq data reported in this paper is GEO: GSE141684. The access number for the whole exome sequencing data reported in this paper is NCBI BioProject: PRJNA607826.
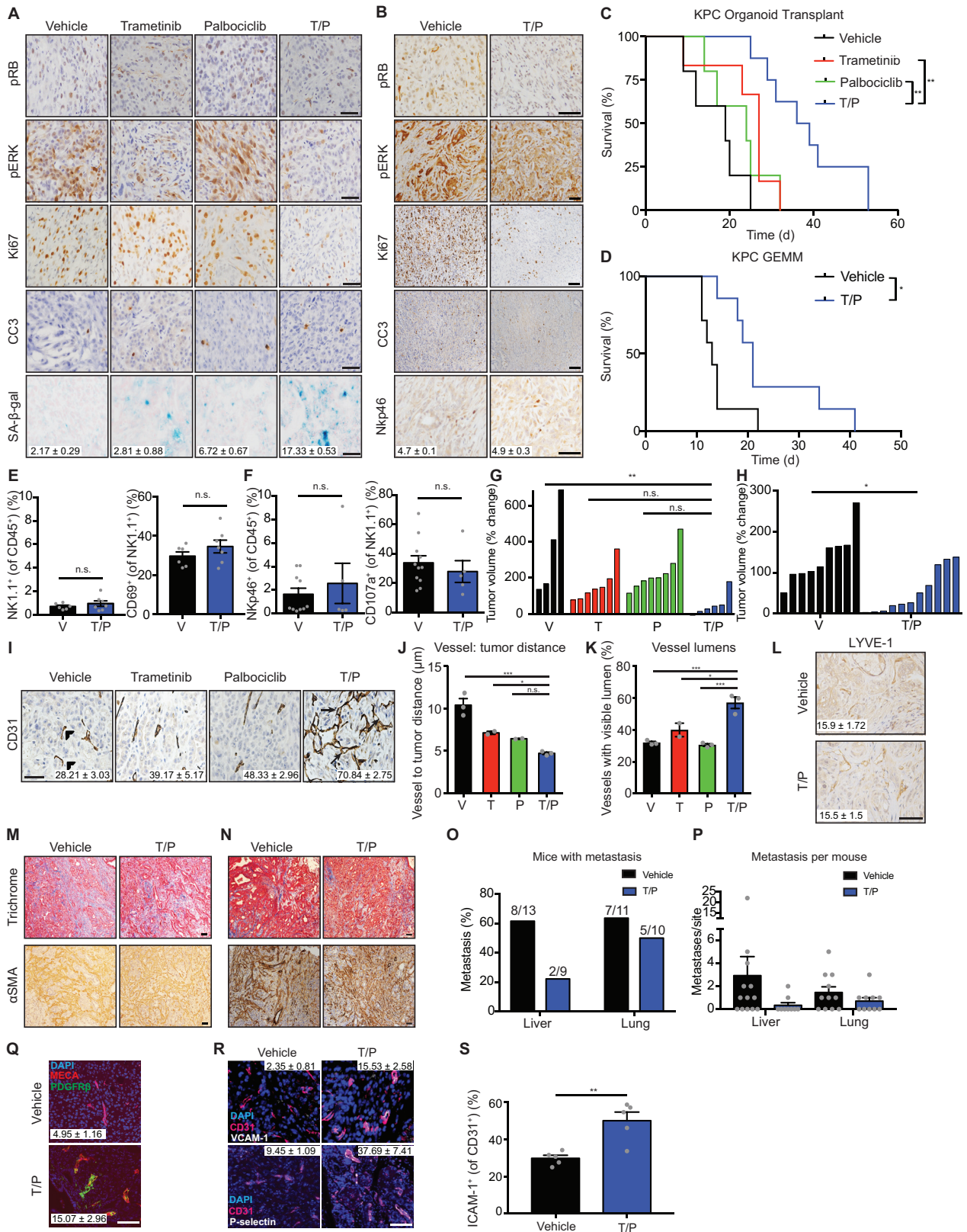
Figure S1. Trametinib and Palbociclib Treatment Does Not Induce NK Cell-Mediated Tumor Responses but Rather Leads to Vascular Remodeling in PDAC Models, Related to Figure 1

(A) Immunohistochemical (IHC) staining and quantification of SA-β-gal positive area in *KPC^mut* organoid transplant tumors treated with vehicle (V), trametinib (T) (1 mg/kg), palbociclib (P) (100 mg/kg), or both (T/P) for 2 weeks (n = 3; T versus T/P and P versus T/P, p < 0.0001).

(B) IHC staining and quantification of NKp46+ NK cells in *KPC^flox* GEMM tumors treated as in (A) (n = 2; p = 0.592).

(C and D) Kaplan-Meier survival curves of *KPC^mut* organoid transplant (C) and *KPC^flox* GEMM (D) mice treated as in (A) (n ≥ 5). Values for V and T/P-treated cohorts in (D) are the same displayed in Figure 3F.

(E and F) Flow cytometry analysis of NK cell numbers and activation in *KPC^mut* transplant (E) or *KPC^flox* GEMM (F) tumors following treatment as in (A) (n ≥ 5).

(G and H) Waterfall plots of the response of *KPC^mut* transplant (G) or *KPC^flox* GEMM (H) tumors following treatment as in (A) (n ≥ 4). Values for V and T/P-treated cohorts in (H) are the same displayed in Figure 3E.

(I–K) IHC staining of *KPC^mut* organoid transplant tumors treated as in (A). Quantification of blood vessels per field (T versus T/P and P versus T/P, p < 0.01) (I), vessel to tumor distance (J), and vessels with visible lumens (K) is shown (n = 3). Arrowhead, collapsed vessel; Arrow, visible lumen.

(L) IHC staining of *KPC^flox* GEMM tumors following treatment as in (A) (n = 3; p = 0.88).

(M and N) IHC staining of *KPC^flox* GEMM (M) or *KPC^mut* organoid transplant (N) tumors following treatment as in (A).

(O and P) PDAC-bearing *KPC^flox* GEMM mice were treated with vehicle or trametinib (1 mg/kg) and palbociclib (100 mg/kg) until survival endpoint, and the lungs and liver were subsequently analyzed for the presence (O) and number (P) of macrometastases (n ≥ 9).

(Q and R) Immunofluorescence (IF) staining and quantification of PDGFRβ (Q) and P-selectin and VCAM-1 (R) colocalization with blood vessels in *KPC^mut* organoid transplant tumors treated as in (A) (n = 2-3; p = 0.0322, 0.0644, and 0.0396, respectively).

(S) Flow cytometry analysis of ICAM-1 expression on endothelial cells in *KPC^mut* organoid transplant tumors following treatment as in (A) (n = 5).

One-way ANOVA (A, G, and I–K). Log-rank test (C and D). Error bars, mean ± SEM. ***p < 0.001, **p < 0.01, *p < 0.05. n.s., not significant. Scale bars, 50 μm.
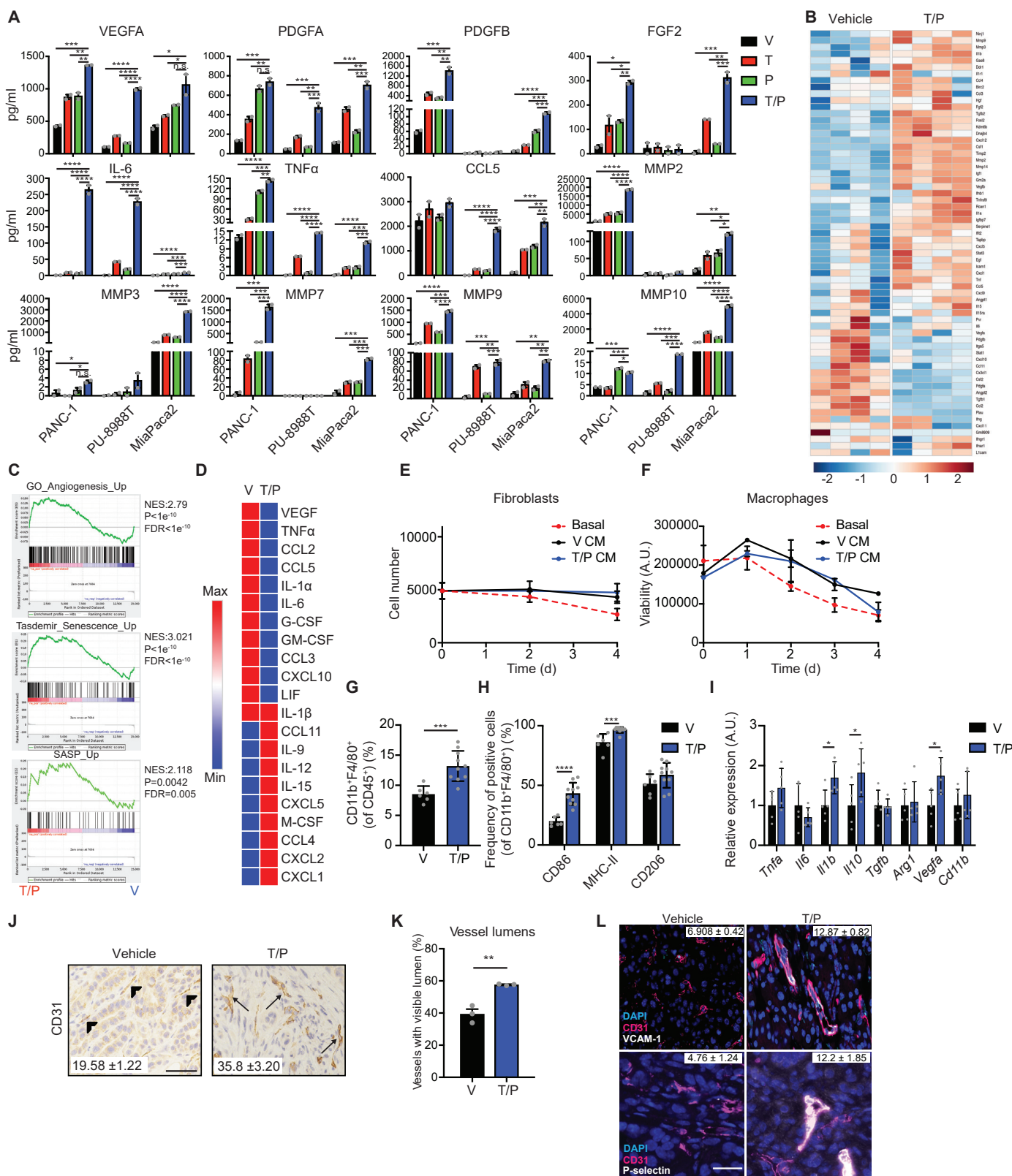
(legend on next page)

Figure S2. Therapy-Induced Senescence Triggers a Pro-angiogenic SASP Exclusively in PDAC Tumor Cells, Related to Figure 2

(A) Cytokine array results from human KRAS mutant PDAC lines treated for 8 days with trametinib (25 nM) and/or palbociclib (500 nM) (n = 2).

(B) Heatmap of RNA-seq analysis of SASP gene expression in tumors cells sorted from KPC^{mut} cell transplant mice treated for 2 weeks with vehicle or trametinib (1 mg/kg) and palbociclib (P) (100 mg/kg) (n = 4).

(C) Gene Set Enrichment Analysis (GSEA) of RNA-seq data from (B). NES, normalized enrichment score.

(D) Heatmap of cytokine array results from primary murine pancreatic fibroblasts following treatment as in (A). Data presented as mean of three biological replicates.

(E and F) Cell growth analysis of fibroblasts (E) or macrophages (F) harvested from C57BL/6 mice and cultured in basal or conditioned media from KPC^{mut} tumor cells treated for 8 days as in (A) (n = 3).

(G and H) Flow cytometry analysis of F4/80$^+$ macrophage numbers and polarization in KPC^{mut} cell transplant tumors following 2-week treatment with vehicle or trametinib (1 mg/kg) and palbociclib (100 mg/kg) (n = 5).

(I) qRT-PCR analysis of M1 (*Tnfa, Il6, Il1b*), M2 (*Il10, Tgfb, Arg1*), and *Vegfa* gene expression in macrophages sorted from KPC^{mut} cell transplant tumors treated as in (G) (n = 5). Cd11b was used as a macrophage loading control. A.U., arbitrary units.

(J and K) IHC staining and quantification of total blood vessels (p = 0.009) (J) and those with visible lumens (K) in tumors harvested from KPC^{mut} organoids transplanted into NOD-*scid* IL2Rγ^{null} (NSG) mice treated as in (G) (n = 3).

(L) IF staining and quantification of P-selectin (p = 0.039) or VCAM-1 (p = 0.0126) colocalization with blood vessels in tumors from (J) (n = 4).

One-way ANOVA (A). Error bars, mean ± SEM. ****p < 0.0001, ***p < 0.001, **p < 0.01, *p < 0.05. n.s., not significant. Scale bars, 50 μm.
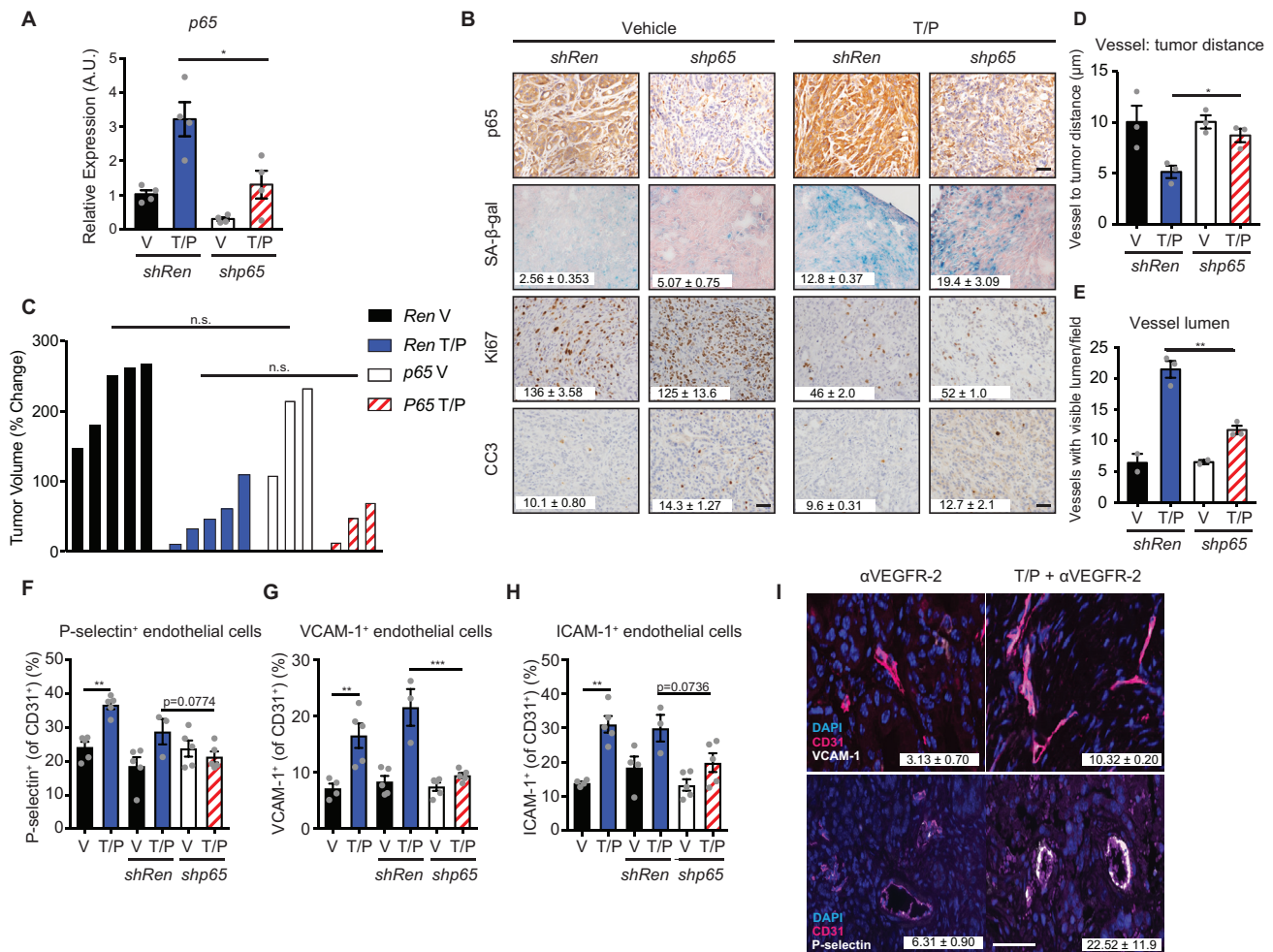
Figure S3. Multiple SASP Factors Contribute to Divergent Vascular Remodeling Phenotypes following T/P Treatment, Related to Figure 2

(A) qRT-PCR analysis of *p65* gene expression in *KPC^mut* cells harboring *Renilla* (*Ren*) or *p65* shRNAs and treated for 8 days with vehicle or trametinib (25nM) and palbociclib (500nM). A.U., arbitrary units.

(B) IHC staining of *KPC^mut* organoid transplant tumors harboring *Ren* or *p65* shRNAs and treated for 2 weeks with vehicle or trametinib (1 mg/kg) and palbociclib (100 mg/kg) (n = 2-3).
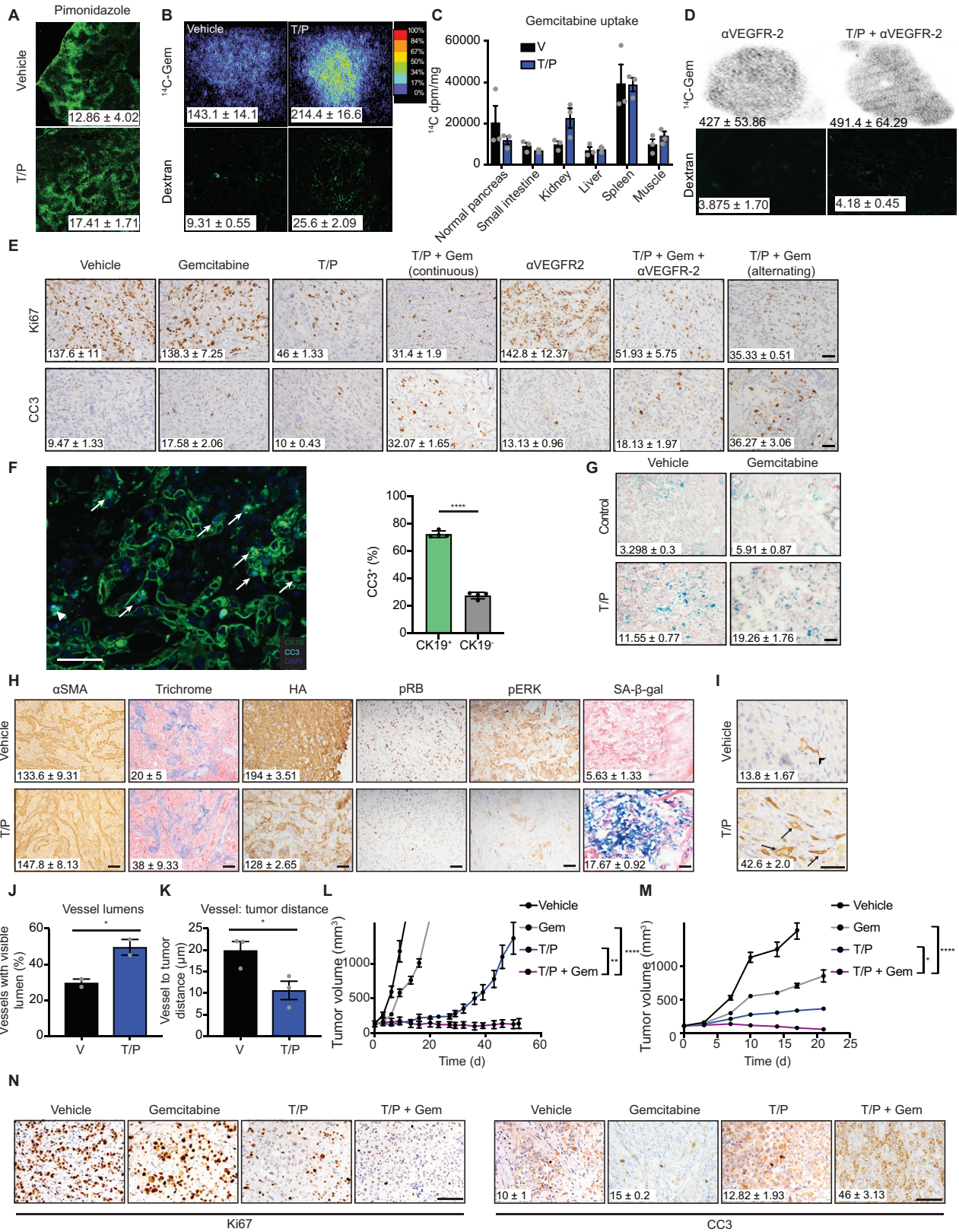
(C) Waterfall plot of the response of *KPC^mut* organoid transplant tumors harboring *Ren* or *p65* shRNAs following treatment as in (B) (n ≥ 3).

(D and E) Quantification of vessel to tumor distance (D) and vessels with visible lumens per field (E) in *KPC^mut* organoid transplant tumors harboring *Ren* or *p65* shRNAs and treated as in (B) (see Figure 2E) (n = 2-3).

(F–H) Flow cytometry analysis of surface marker expression on endothelial cells in indicated *KPC^mut* cell transplant tumors treated as in (B) (n = 3-5).

(I) IF staining and quantification of P-selectin (p = 0.17) or VCAM-1 (p = 0.01) colocalization with blood vessels in *KPC^mut* organoid transplant tumors treated for 2 weeks with vehicle, trametinib (1 mg/kg), palbociclib (100 mg/kg), and/or a VEGFR-2 blocking antibody (DC101; 800 μg) (n = 4).

One-way ANOVA (C–H). Error bars, mean ± SEM. ***p < 0.001, **p < 0.01, *p < 0.05. n.s., not significant. Scale bars, 50 μm.

A Pimonidazole

Vehicle
12.86 ± 4.02

T/P
17.41 ± 1.71

B
Vehicle | T/P
¹⁴C-Gem
143.1 ± 14.1 | 214.4 ± 16.6

Dextran
9.31 ± 0.55 | 25.6 ± 2.09

100%
84%
67%
50%
34%
17%
0%

C Gemcitabine uptake
¹⁴C dpm/mg
■ V
■ T/P
Normal pancreas, Small intestine, Kidney, Liver, Spleen, Muscle

D
αVEGFR-2 | T/P + αVEGFR-2
¹⁴C-Gem
427 ± 53.86 | 491.4 ± 64.29

Dextran
3.875 ± 1.70 | 4.18 ± 0.45

E
| | Vehicle | Gemcitabine | T/P | T/P + Gem (continuous) | αVEGFR2 | T/P + Gem + αVEGFR-2 | T/P + Gem (alternating) |
Ki67
137.6 ± 11 | 138.3 ± 7.25 | 46 ± 1.33 | 31.4 ± 1.9 | 142.8 ± 12.37 | 51.93 ± 5.75 | 35.33 ± 0.51

CC3
9.47 ± 1.33 | 17.58 ± 2.06 | 10 ± 0.43 | 32.07 ± 1.65 | 13.13 ± 0.96 | 18.13 ± 1.97 | 36.27 ± 3.06

F
CK19
CC3
DAPI

CC3⁺ (%)
CK19⁺ | CK19⁻
****

G
| | Vehicle | Gemcitabine |
Control
3.298 ± 0.3 | 5.91 ± 0.87

T/P
11.55 ± 0.77 | 19.26 ± 1.76

H
| | αSMA | Trichrome | HA | pRB | pERK | SA-β-gal |
Vehicle
133.6 ± 9.31 | 20 ± 5 | 194 ± 3.51 | | | 5.63 ± 1.33

T/P
147.8 ± 8.13 | 38 ± 9.33 | 128 ± 2.65 | | | 17.67 ± 0.92

I
Vehicle
13.8 ± 1.67

T/P
42.6 ± 2.0

J Vessel lumens
Vessels with visible lumen (%)
V | T/P
*

K Vessel: tumor distance
Vessel to tumor distance (μm)
V | T/P
*

L
Tumor volume (mm³)
Time (d)
→ Vehicle
→ Gem
→ T/P
→ T/P + Gem
**
****

M
Tumor volume (mm³)
Time (d)
→ Vehicle
→ Gem
→ T/P
→ T/P + Gem
*
****

N
| Vehicle | Gemcitabine | T/P | T/P + Gem | | Vehicle | Gemcitabine | T/P | T/P + Gem |
Ki67
CC3
10 ± 1 | 15 ± 0.2 | 12.82 ± 1.93 | 46 ± 3.13

Figure S4. Trametinib and Palbociclib Treatment Enhances Gemcitabine Cytotoxicity in Both Mouse and Human PDAC via Vascular Remodeling, Related to Figure 3

(A) IF staining and quantification of activated pimonidazole in KPC^{mut} organoid transplant tumors treated with vehicle or trametinib (1 mg/kg) and palbociclib (100 mg/kg) for 2 weeks (n = 2; p = 0.41).

(B) KPC^{flox} GEMM mice were pretreated with vehicle or trametinib (1 mg/kg) and palbociclib (100 mg/kg) for 2 weeks, and subsequently injected with ^{14}C-labeled gemcitabine (Gem) and dextran prior to tissue harvest. Heatmap representation of autoradiograph showing distribution and quantification of ^{14}C-Gem uptake into tumors (n = 3; p = 0.03). Below: dextran staining and quantification (n = 3-4; p = 0.0003).

(C) Quantification of ^{14}C-Gem levels in indicated tissues harvested from KPC^{mut} organoid transplant mice following treatment as in (B) (n = 3).

(D) KPC^{mut} organoid transplant mice were pretreated with vehicle, trametinib (1 mg/kg), palbociclib (100 mg/kg), and/or a VEGFR-2 blocking antibody (DC101; 800 μg) for 2 weeks, and subsequently injected with ^{14}C-labeled gemcitabine and dextran prior to tissue harvest. Autoradiograph showing distribution and quantification of ^{14}C-Gem uptake into tumors (n = 2-3; p = 0.485). Below: dextran staining and quantification (n = 2-3; p = 0.844).

(E) IHC staining of KPC^{mut} organoid transplant tumors treated for 2 weeks with vehicle, trametinib (1 mg/kg), palbociclib (100 mg/kg), gemcitabine (100 mg/kg), and/or a VEGFR-2 blocking antibody (DC101; 800 μg) either continuously (C) or on an alternating (A) schedule. Quantification of Ki67^{+} (Gem versus T/P/G (C), p = 0.0244; Gem versus T/P/G (A), p = 0.0029; T/P/G (C) versus T/P/G/DC101, p = 0.0727) and cleaved caspase-3 (CC3^{+}) cells (Gem versus T/P/G (C), p = 0.0054; Gem versus T/P/G (A), p = 0.0072; T/P/G (C) versus T/P/G/DC101, p = 0.0056) per field is shown (n = 3).

(F) IF staining of a KPC^{flox} GEMM tumors treated for 2 weeks with trametinib (1 mg/kg), palbociclib (100 mg/kg), and gemcitabine (100 mg/kg). Right: quantification of the percentage of CC3^{+} cells in the epithelial (CK19^{+}) versus stromal (CK19^{-}) compartments (n = 4).

(G) Staining and quantification of SA-β-gal positive area in KPC^{mut} organoid transplant tumors treated for 2 weeks with vehicle, trametinib (1 mg/kg), palbociclib (100 mg/kg), and/or gemcitabine (100 mg/kg) (n = 3; T/P versus T/P/G, p = 0.0183).

(H) IHC staining of PR-07 patient-derived xenograft (PDX) PDAC tumors treated as in (A). Quantification of αSMA (p = 0.3140), collagen (trichrome) (p = 0.2312), and hyaluronic acid (HA) (p = 0.0001) staining intensity, as well as SA-β-gal positive area (p = 0.0017), is shown (n = 3).

(I–K) IHC staining and quantification of blood vessels per field (p = 0.0004) (I), vessel to tumor distance (J), and vessels with visible lumens (K) in PR-07 PDX PDAC tumors treated as in (A). Arrowhead, collapsed vessel; Arrow, visible lumen.

(L and M) Tumor volumes of mice bearing PR-07 (L) or PR-05 (M) PDAC PDX tumors treated with vehicle, trametinib (1 mg/kg), palbociclib (100 mg/kg), and/or gemcitabine (100 mg/kg) for indicated times (n = 7).

(N) IHC staining and quantification of CC3^{+} cells in PR-07 PDAC PDX tumors treated as in (L) (n = 3; T/P versus T/P/G, p = 0.0046).

One-way ANOVA (E and G). Two-way ANOVA (L and M). Error bars, mean ± SEM. ****p < 0.0001, **p < 0.01, *p < 0.05. Scale bars, 50 μm.
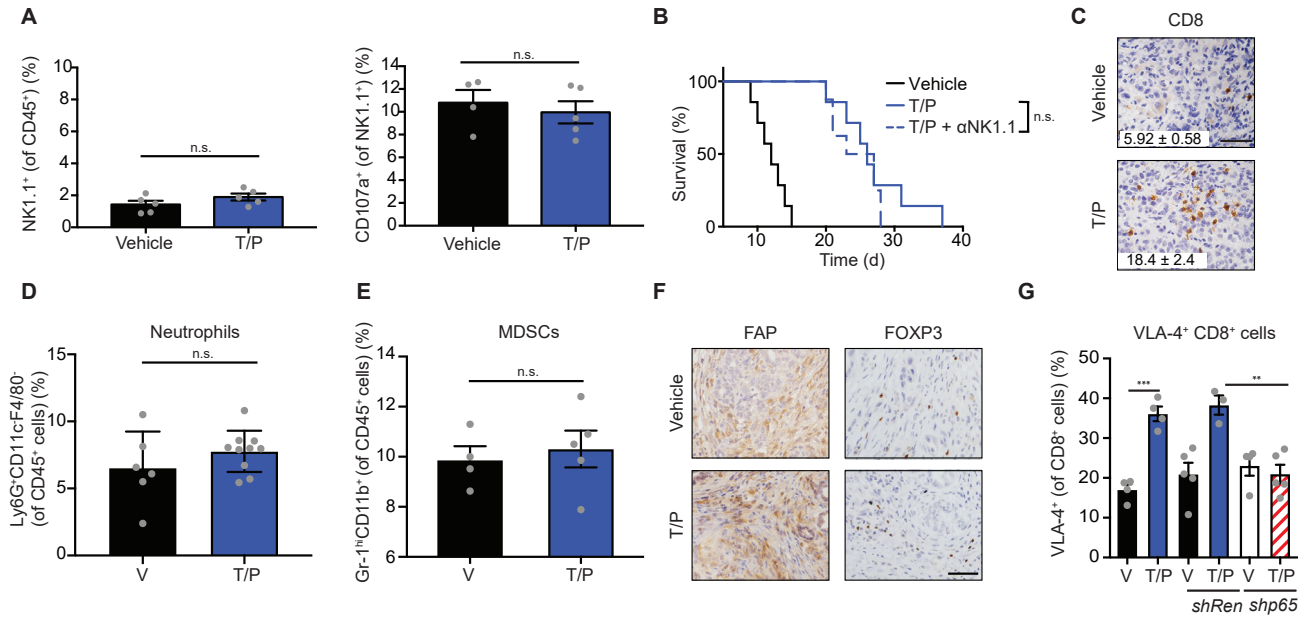
Figure S5. Therapy-Induced Senescence Directly Promotes CD8⁺ T Cell Accumulation in PDAC, Related to Figure 4

(A) Flow cytometry analysis of NK cell numbers (left) and activity (right) in *KPC^mut* cell transplant tumors following 2-week treatment with vehicle or trametinib (1 mg/kg) and palbociclib (100 mg/kg) (n = 4-5).

(B) Kaplan-Meier survival curve of *KPC^mut* cell transplant mice treated with vehicle or trametinib (1 mg/kg) and palbociclib (100 mg/kg) in the presence or absence of a NK1.1 depleting antibody (PK136; 250 ug) (n ≥ 7).

(C) IHC staining and quantification of CD8⁺ T cells per field in *KPC^mut* organoid transplant tumors treated as in (A) (n = 2-3; p = 0.037).

(D and E) Flow cytometry analysis of neutrophils (D) and MDSCs (E) in *KPC^mut* cell transplant tumors treated as in (A) (n = 4-5).

(F) IHC staining of *KPC^mut* organoid transplant tumors treated as in (A). Representative images of 3 biological replicates.

(G) Flow cytometry analysis of VLA-4 expression on CD8⁺ T cells in indicated *KPC^mut* cell transplant tumors treated as in (A) (n = 3-5).

One-way ANOVA (G). Log-rank test (B). Error bars, mean ± SEM. ***p < 0.001, **p < 0.01. n.s., not significant. Scale bars, 50 μm.
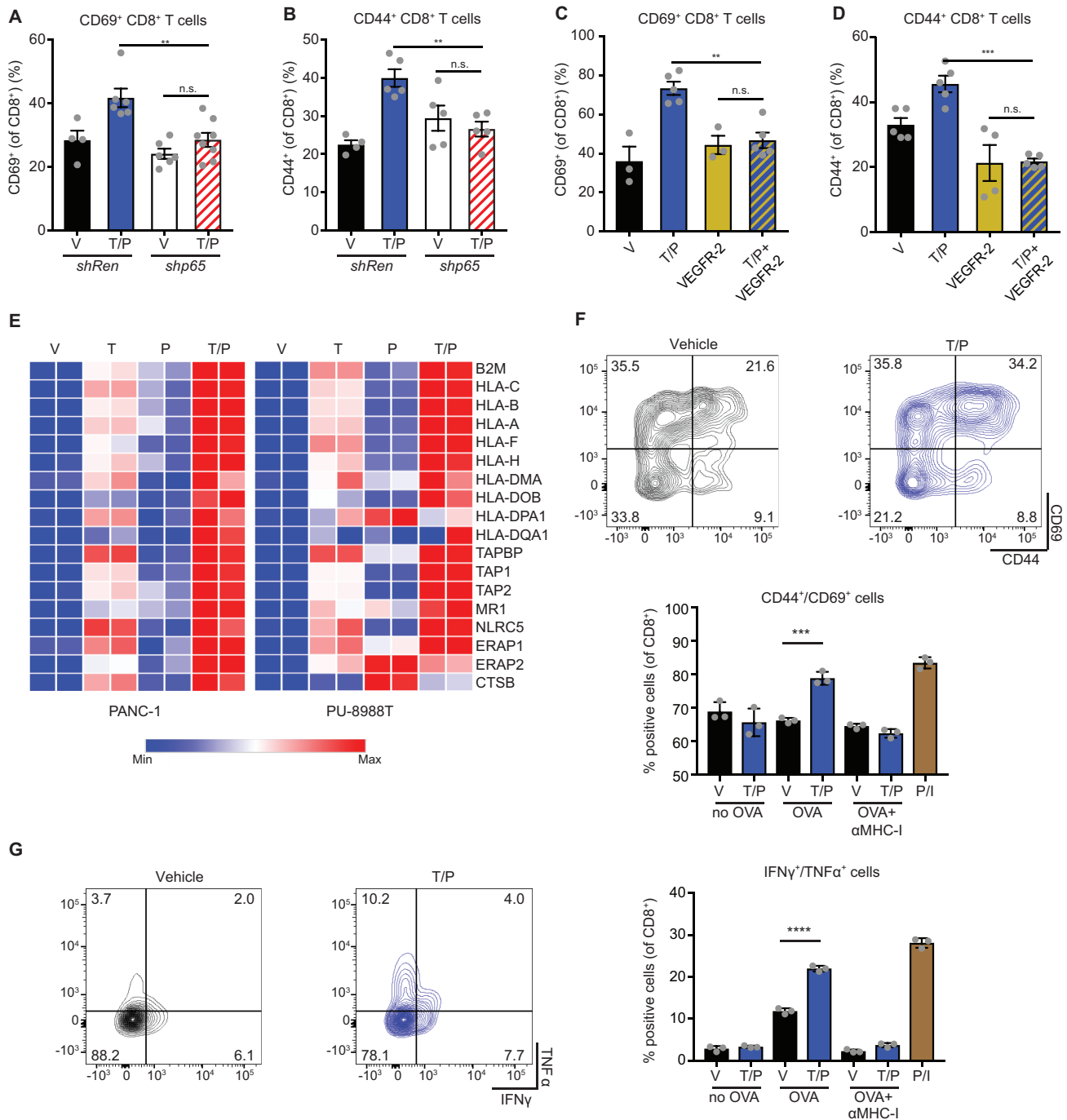
Figure S6. Therapy-Induced Senescence Stimulates CD8+ T Cell Activation, Related to Figure 5

(A and B) Flow cytometry analysis of CD8+ T cells in *KPCmut* PDAC cell transplant tumors harboring control *Ren* or *p65*-targeting shRNAs and treated with vehicle or trametinib (1 mg/kg) and palbociclib (100 mg/kg) for 2 weeks (n = 4-5 mice).

(C and D) Flow cytometry analysis of CD8+ T cells in *KPCmut* cell transplant tumors treated with vehicle, trametinib (1 mg/kg), palbociclib (100 mg/kg), and/or a VEGFR-2 blocking antibody (DC101; 800 μg) for 2 weeks (n = 3-5).

(E) Heatmap of expression of genes related to antigen processing and presentation in human KRAS mutant PDAC lines following 8 day treatment with trametinib (25 nM) and/or palbociclib (500 nM) as assessed from analysis of RNA-seq data generated in Ruscetti et al. (2018). Two biological replicates per cell line are shown.

(legend continued on next page)

(F and G) Reprentative histograms and quantification of T cell activation (F) and effector function (G) markers following flow cytometry analysis of OTI CD8$^+$ T cells co-cultured with control or chicken ovalbumin (OVA)-expressing KPC^{mut} tumor cells pretreated with vehicle or trametinib (25 nM) and palbociclb (500 nM) for 8 days. PMA/ionomycin (P/I) stimulation served as a positive control for T cell activation, and MHC-I activity was functionally blocked with an H-2k^b blocking antibody (Y-3; 40 μg/ml) (n = 3).

One-way ANOVA (A–D, F, and G). Error bars, mean ± SEM. ****$p < 0.0001$, ***$p < 0.001$, **$p < 0.01$. n.s., not significant.
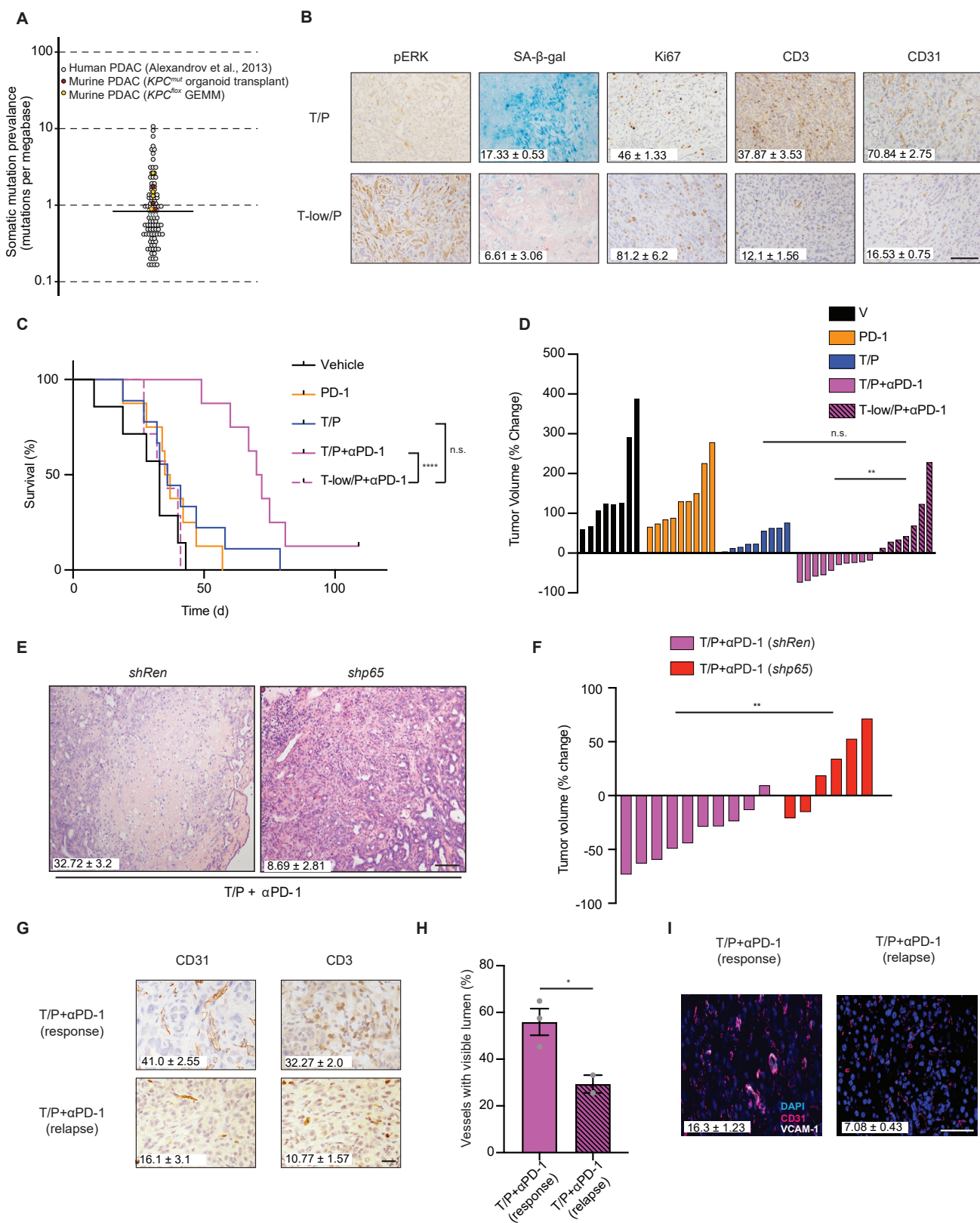
Figure S7. Synergy between T/P Treatment and PD-1 Checkpoint Blockade Is Dependent on SASP-Mediated Vascular Remodeling, Related to Figure 7

(A) Quantification of number of somatic mutations (per megabase) in KPC^{flox} GEMM (yellow dots; n = 4) and KPC^{mut} organoid transplant tumors (red dots; n = 3) as compared to human PDAC tumors (gray dots) from Alexandrov et al. (2013).

(B) IHC staining and quantification of SA-β-gal$^+$ (p = 0.0028), Ki67$^+$ (p = 0.031), CD3$^+$ (p = 0.0026), and CD31$^+$ (p < 0.0001) cells per field in KPC^{mut} organoid transplant tumors treated with palbociclib (100 mg/kg) in combination with standard (1 mg/kg) and low dose (T-low) (0.3 mg/kg) trametinib (n = 2-3). Values for SA-β-gal, CD31, and Ki67 in the T/P-treated cohort are the same displayed in Figures S1A, S1I, and S4E.

(C) Kaplan-Meier survival curve of KPC^{mut} PDAC organoid transplant mice treated with vehicle, trametinib (1 or 0.3 (T-low) mg/kg), palbociclib (100 mg/kg), and/or a PD-1 blocking antibody (RMP1-14; 200 μg) (n ≥ 7). Values for V, T/P, PD-1, and T/P/PD-1-treated cohorts are the same displayed in Figure 7F.

(D) Waterfall plot of the response of KPC^{mut} PDAC organoid transplant tumors after 2 weeks of treatment as in (C) (n ≥ 7). Values for V, T/P, PD-1, and T/P/PD-1-treated cohorts are the same displayed in Figure 7D.

(E and F) KPC^{mut} organoid transplant tumors harboring Ren or $p65$ shRNAs were treated for 2 weeks with trametinib (1 mg/kg), palbociclib (100 mg/kg), and a PD-1 blocking antibody (RMP1-14; 200 μg). (E) H&E staining and quantification of percent of tumor covered in necrosis (n = 2-3; p = 0.03). (F) Waterfall plot of the response of individual tumors to treatment (n ≥ 6).

(G–I) IHC and IF staining of KPC^{mut} organoid transplant tumors following acute 2 week treatment (response) or > 80 days of treatment (relapse) with trametinib (1 mg/kg), palbociclib (100 mg/kg), and a PD-1 blocking antibody (RMP1-14; 200 μg). (G) Quantification of CD31$^+$ (p = 0.0085) and CD3$^+$ (p = 0.0048) cells per field (n = 2-3). (H) Quantification of blood vessels with visible lumens (n = 2-3). (I) Quantification of VCAM-1 (p = 0.0195) colocalization with blood vessels (n = 4).

One-way ANOVA (D). Log-rank test (C). Error bars, mean ± SEM. ****p < 0.0001, **p < 0.01, *p < 0.05. n.s., not significant. Scale bars, 50 μm.